

# 1 **Historical (1960–2014) lightning and LNO<sub>x</sub> trends and their** 2 **controlling factors in a chemistry–climate model**

3 Yanfeng He<sup>1</sup>, Kengo Sudo<sup>1,2</sup>

4 <sup>1</sup> Graduate School of Environment Studies, Nagoya University, Nagoya, 464-8601, Japan

5 <sup>2</sup> Japan Agency for Marine–Earth Science and Technology (JAMSTEC), Yokohama, 237-0061, Japan

6 *Correspondence to:* Yanfeng He (hyf412694462@gmail.com)

7 **Abstract.** Lightning can cause natural hazards that result in human and animal injuries or fatalities, infrastructure destruction,  
8 and wildfire ignition. Lightning-produced NO<sub>x</sub> (LNO<sub>x</sub>), a major NO<sub>x</sub> (NO<sub>x</sub>=NO+NO<sub>2</sub>) source, plays a vital role in  
9 atmospheric chemistry and global climate. The Earth has experienced marked global warming and changes in aerosol and  
10 aerosol precursor emissions (AeroPEs) since the 1960s. Investigating long-term historical (1960–2014) lightning and LNO<sub>x</sub>  
11 trends can provide important indicators for all lightning-related phenomena and for LNO<sub>x</sub> effects on atmospheric chemistry  
12 and global climate. Understanding how global warming and changes in AeroPEs influence historical lightning–LNO<sub>x</sub> trends  
13 can be helpful in providing a scientific basis for assessing future lightning–LNO<sub>x</sub> trends. Moreover, global lightning  
14 activities' responses to large volcanic eruptions such as the 1991 Pinatubo eruption are not well elucidated, and are worth  
15 exploring. This study employed the widely used cloud top height lightning scheme (CTH scheme) and the newly developed  
16 ice-based ECMWF-McCAUL lightning scheme to investigate historical (1960–2014) lightning–LNO<sub>x</sub> trends and variations  
17 and their influencing factors (global warming, increases in AeroPEs, and Pinatubo eruption) in the framework of the  
18 CHASER (MIROC) chemistry–climate model. Results of sensitivity experiments indicate that both lightning schemes  
19 simulated almost flat global mean lightning flash rate trends during 1960–2014 in CHASER. Moreover, both lightning  
20 schemes suggest that past global warming enhances historical trends of global mean lightning density and global LNO<sub>x</sub>  
21 emissions in a positive direction (around 0.03% yr<sup>-1</sup> or 3% K<sup>-1</sup>). However, past increases in AeroPEs exert an opposite effect  
22 to the lightning–LNO<sub>x</sub> trends (-0.07% yr<sup>-1</sup> – -0.04% yr<sup>-1</sup> for lightning and -0.08% yr<sup>-1</sup> – -0.03% yr<sup>-1</sup> for LNO<sub>x</sub>) when one  
23 considers only the aerosol radiative effects in the cumulus convection scheme. Additionally, effects of past global warming  
24 and increases in AeroPEs on lightning trends were found to be heterogeneous across different regions when analyzing  
25 lightning trends on the global map. Lastly, this report is the first of study results suggesting that global lightning activities  
26 were suppressed markedly during the first year after the Pinatubo eruption shown in both lightning schemes (global lightning  
27 activities decreased by as much as 18.10% simulated by the ECMWF-McCAUL scheme). Based on simulated suppressed  
28 lightning activities after the Pinatubo eruption, findings also indicate that global LNO<sub>x</sub> emissions decreased after the 2–3-  
29 year Pinatubo eruption (1.99%–8.47% for the annual percentage reduction). Model intercomparisons of lightning flash rate  
30 trends and variations between our study (CHASER) and other Coupled Model Intercomparison Project Phase 6 (CMIP6)  
31 models indicate great uncertainties in historical (1960–2014) global lightning trend simulations. Such uncertainties must be  
32 investigated further.

### 33 **1 Introduction**

34 Lightning, an extremely energetic natural phenomenon, occurs at every moment somewhere on Earth: its average occurrence  
35 frequency is approximately 46 times per second (Cecil et al., 2014). Lightning generation is associated with electric charge  
36 separation, which is mainly realized by collisions between graupel and hail and hydrometeors of other types within  
37 convective clouds (Lopez, 2016). As a natural hazard, lightning can cause human and animal injuries and fatalities,  
38 infrastructure destruction, and wildfire ignition (Cerveny et al., 2017; Cooper and Holle, 2019; Jensen et al., 2022;  
39 Veraverbeke et al., 2022). Lightning-produced  $\text{NO}_x$  ( $\text{LNO}_x$ ) accounts for around 10% of the global tropospheric  $\text{NO}_x$   
40 ( $\text{NO}_x = \text{NO} + \text{NO}_2$ ) source. It is regarded as the dominant  $\text{NO}_x$  source in the middle to upper troposphere (Schumann and  
41 Huntrieser, 2007; Finney et al., 2016b). Moreover,  $\text{LNO}_x$  plays a crucially important role in atmospheric chemistry and  
42 global climate by affecting the abundances of OH radical, important greenhouse gases (GHGs) such as ozone and methane,  
43 and other trace gases (Labrador et al., 2005; Schumann and Huntrieser, 2007; Wild, 2007; Liaskos et al., 2015; Finney et al.,  
44 2016a; Murray, 2016; Tost, 2017; He et al., 2022b).

45  
46 Reportedly, the lightning flash rate (LFR) is related to the stage of convective cloud development (Williams et al., 1989),  
47 Convective Available Potential Energy (CAPE) (Romps et al., 2014), cloud liquid–ice water content (Saunders et al., 1991;  
48 Finney et al., 2014) and even to the convective precipitation volume (Goodman et al., 1990; McCaul et al., 2009; Romps et  
49 al., 2014). Long-term global warming is associated with changes in the overall temperature and relative humidity profiles in  
50 the atmosphere and global convective adjustment (Manabe and Wetherald, 1975; Del Genio et al., 2007), which can strongly  
51 affect the lightning-related factors described above. Consequently, long-term global warming can be a fundamentally  
52 important factor affecting long-term variations in global lightning activity. Findings from many earlier numerical simulation  
53 studies manifest that global lightning activities are sensitive to long-term global warming, with most studies showing 5–16%  
54 (average around 10%) increases in global lightning activities per 1 K global warming (Price and Rind, 1994; Zeng et al.,  
55 2008; Hui and Hong, 2013; Banerjee et al., 2014; Krause et al., 2014; Romps et al., 2014; Clark et al., 2017). However, other  
56 numerical simulation studies such as those using an ice-based lightning scheme or convective mass flux as a proxy to  
57 parameterize lightning have yielded opposite results, suggesting that global lightning activity will decrease under long-term  
58 global warming (Clark et al., 2017; Finney et al., 2018).

59  
60 Aside from long-term global warming, changes in aerosol loading can also be responsible for long-term global lightning  
61 activity variations. Aerosols influence lightning activity through aerosol radiative and microphysical effects, but the degree  
62 to which the two distinct effects influence regional or global scale lightning activities remains unclear (Yuan et al., 2011;  
63 Yang et al., 2013; Tan et al., 2016; Altaratz et al., 2017; Wang et al., 2018; Liu et al., 2020). Further research is needed. It is  
64 urgently necessary to elucidate the effects of aerosol radiative and microphysical effects on lightning on a global scale. The  
65 aerosol radiative effects indicate that aerosols can heat the atmospheric layer and can cool the Earth's surface by absorbing

66 and scattering solar radiation (Kaufman et al., 2002; Koren et al., 2004, 2008; Li et al., 2017). Thereby, convection and  
67 electrical activities are likely to be inhibited (Koren et al., 2004; Yang et al., 2013; Tan et al., 2016). The microphysical  
68 effects suggest that by acting as cloud condensation nuclei (CCN) or as ice nuclei, aerosols can reduce the mean size of  
69 cloud droplets, consequently suppressing the coalescence of cloud droplets into raindrops. As a result, more liquid water  
70 particles are uplifted to higher mixed-phase regions of the troposphere, where they invigorate lightning (Wang et al., 2018;  
71 Liu et al., 2020).

72

73 The Earth has experienced a considerable degree of global warming and changes in AeroPEs since the 1960s (Hoesly et al.,  
74 2018; Climate at a Glance | National Centers for Environmental Information (NCEI), 2022). However, how historical  
75 lightning has trended and how lightning has responded to historical global warming and changes in AeroPEs are not well  
76 examined. This topic is worth exploring because historical lightning densities are indicators for all lightning-related  
77 phenomena (Price and Rind, 1994). Exploring the historical global LNO<sub>x</sub> emission trend is also meaningful because it can  
78 indicate the effects of LNO<sub>x</sub> emissions on atmospheric chemistry and global climate. Furthermore, investigating the effects  
79 of historical global warming and increases in AeroPEs on historical lightning–LNO<sub>x</sub> trends can provide a basis for assessing  
80 future lightning–LNO<sub>x</sub> trends.

81

82 Large-scale volcanic eruptions such as the 1991 Pinatubo eruption inject tremendous amounts of sulfuric gas into the  
83 stratosphere, where it converts to H<sub>2</sub>SO<sub>4</sub> aerosols. Consequently, the stratospheric aerosols have increased in abundance after  
84 the volcanic eruptions. The enhanced stratospheric aerosol layer can cool the Earth's surface heterogeneously and can  
85 decrease the total amount of water in the atmosphere (Soden et al., 2002; Boucher, 2015, p.63). The near-global  
86 perturbations in the radiative energy balance and meteorological fields caused by such strong volcanic eruptions might  
87 influence global lightning activities. If so, there might be ramifications for all lightning-related phenomena. Nevertheless,  
88 they remain poorly understood.

89

90 In our earlier work, we developed a new process and ice-based lightning scheme called the ECMWF-McCAUL scheme (He  
91 et al., 2022b). This lightning scheme was developed by combining benefits of the lightning scheme used in the European  
92 Centre for Medium-Range Weather Forecasts (ECMWF) forecasting system (Lopez, 2016) and those presented in reports by  
93 McCaul et al. (McCaul et al., 2009). The ECMWF-McCAUL scheme simulated the best lightning density spatial  
94 distributions among four existing lightning schemes when compared against satellite lightning observations (Lightning  
95 Imaging Sensor (LIS) and Optical Transient Detector (OTD)) during 2007–2011. The sensitivity of global lightning activity  
96 to changes in surface temperature on a decadal timescale was estimated as 10.13% K<sup>-1</sup> using the ECMWF-McCAUL scheme  
97 (He et al., 2022b), which is close to most past estimates (average around 10% K<sup>-1</sup>).

98

99 Using a chemistry–climate model CHASER (MIROC) with two lightning schemes (the widely used cloud top height scheme  
100 and the ice-based ECMWF-McCAUL scheme), we investigated historical lightning–LNO<sub>x</sub> trends quantitatively and  
101 ascertained how global warming, increases in AeroPEs, and the Pinatubo eruption respectively influenced them. Using two  
102 lightning schemes, we demonstrated the sensitivities of different lightning schemes to historical global warming, increases in  
103 AeroPEs, and the Pinatubo eruption.

104

105 Research methods including the model description and experiment setup, are described in Sect. 2. In Sect. 3.1, the simulated  
106 historical lightning distributions and trends are validated using LIS/OTD lightning observations. Section 3.2 presents the  
107 effects of global warming and increases in AeroPEs on historical lightning–LNO<sub>x</sub> trends. In Sect. 3.3, the Pinatubo volcanic  
108 eruption effects on historical lightning–LNO<sub>x</sub> trends are discussed. Section 3.4 elucidated model intercomparisons of LFR  
109 trends and variation between our study (CHASER) and other CMIP6 model outputs. Section 4 presents relevant discussions  
110 and conclusions based on these study findings.

## 111 **2 Method**

### 112 **2.1 Chemistry–climate model**

113 We used the CHASER (MIROC) global chemistry–climate model (Sudo et al., 2002; Sudo and Akimoto, 2007; Watanabe et  
114 al., 2011; Ha et al., 2021) for this study, which incorporated consideration of detailed chemical and physical processes in the  
115 troposphere and stratosphere. The CHASER version adopted for this study simulates the distributions of 94 chemical species  
116 while reflecting the effects of 269 chemical reactions (58 photolytic, 190 kinetic, and 21 heterogeneous). As processes  
117 associated with tropospheric chemistry, Non-Methane Hydrocarbons (NMHC) oxidation and the fundamental chemical cycle  
118 of O<sub>x</sub>–NO<sub>x</sub>–HO<sub>x</sub>–CH<sub>4</sub>–CO are considered. CHASER simulates stratospheric chemistry involving the Chapman mechanisms  
119 and catalytic reactions associated with HO<sub>x</sub>, NO<sub>x</sub>, ClO<sub>x</sub>, and BrO<sub>x</sub>. Moreover, it simulates the formation of polar  
120 stratospheric clouds (PSCs) and heterogeneous reactions occurring on their surfaces. CHASER is on-line-coupled to MIROC  
121 AGCM ver. 5.0 (Watanabe et al., 2011), which simulates cumulus convection (Arakawa–Schubert scheme) and grid-scale  
122 large-scale condensation to represent cloud and precipitation processes. The radiation flux is calculated using a two-stream k  
123 distribution radiation scheme, which considers absorption, scattering, and emissions by aerosol and cloud particles as well as  
124 by gaseous species (Sekiguchi and Nakajima, 2008; Goto et al., 2015). The aerosol component in CHASER is coupled with  
125 the SPRINTARS aerosol model (Takemura et al., 2009), particularly for simulating primary organic carbon, sea-salt, and  
126 dust, which is also based on MIROC. The aerosol radiation effects are considered in both large-scale condensation and  
127 cumulus convection schemes, although the aerosol microphysical effects are only reflected in the large-scale condensation  
128 scheme.

129

130 This study used a horizontal resolution of T42 ( $2.8^\circ \times 2.8^\circ$ ), with vertical resolution of 36  $\sigma$ -p hybrid levels from the surface  
 131 to approximately 50 km. Anthropogenic and biomass burning emissions were obtained from the CMIP6 forcing datasets  
 132 (van Marle et al., 2017; Hoesly et al., 2018) for 1959–2014 (<https://esgf-node.llnl.gov/search/input4mips/>, last access: 19  
 133 September 2022). Interannual variation in biogenic emissions for isoprene, monoterpene, acetone, and methanol were  
 134 considered using an off-line simulation by the Vegetation Integrative Simulator for Trace Gases (VISIT) terrestrial  
 135 ecosystem model (Ito and Inatomi, 2012). The residual biogenic emissions (ethane, propane, ethylene, propene) used are  
 136 climatological values derived from the Model of Emissions of Gases and Aerosols from Nature (MEGAN) modeling system  
 137 (Guenther et al., 2012).

138

139 The CHASER (MIROC) global chemistry–climate model originally parameterizes lightning with the widely used cloud top  
 140 height scheme (Price and Rind, 1992). A newly developed ice-based lightning scheme called the ECMWF-McCAUL here  
 141 had been implemented into CHASER (MIROC) (He et al., 2022b). The ECMWF-McCAUL scheme computes LFRs as a  
 142 function of CAPE and  $Q_{Ra}$  ( $Q_{Ra}$  represents the total volumetric amount of cloud ice, graupel, and snow in the charge  
 143 separation region). Compared with the cloud top height, a salient advantage of the ECMWF-McCAUL scheme is that it has a  
 144 direct physical link with the charging mechanism.

## 145 2.2 Lightning NO<sub>x</sub> emission parameterizations

146 We tested two lightning schemes for this study. The first lightning scheme is the widely used cloud top height (CTH) scheme  
 147 (Price and Rind, 1992), which was used originally in CHASER (MIROC). This lightning scheme uses the following  
 148 equations to calculate LFR.

$$149 F_l = 3.44 \times 10^{-5} H^{4.9} \quad (1)$$

$$150 F_o = 6.2 \times 10^{-4} H^{1.73} \quad (2)$$

151 Therein,  $F$  represents the total flash frequency (fl. min<sup>-1</sup>),  $H$  stands for the cloud-top height (km), and subscripts  $l$  and  $o$   
 152 respectively denote the land and ocean (Price and Rind, 1992). Actually, we realize the CTH scheme in CHASER using the  
 153 following equations (Eq. (3) and Eq. (4)). Each model layer’s cumulus cloud fractions are used to weight the calculated  
 154 lightning densities from that layer in the CTH scheme.

$$155 F_l = \sum_{i=1}^{n=36} adj\_factor \times Cu\_CF_i \times (H_i - H_{surface})^{4.9} \quad (3)$$

$$156 F_o = \sum_{i=1}^{n=36} adj\_factor \times Cu\_CF_i \times (H_i - H_{surface})^{1.73} \quad (4)$$

157 In those equations,  $i$  represents the model layer index. In addition,  $adj\_factor$  represents adjustment factors that differ for  
 158 different model layers and model grids.  $Cu\_CF_i$  symbolizes the cumulus cloud fraction at model layer  $i$ .  $H_i$  and  $H_{surface}$   
 159 respectively denote the altitude of model layer  $i$  and the altitude of the model’s surface layer.

160

161 The second lightning scheme used for this study is a newly developed one named the ECMWF-McCAUL scheme (He et al.,  
 162 2022b), which is based on the original ECMWF scheme and findings reported by McCaul et al. (2009). The ECMWF-  
 163 McCAUL scheme calculates LFRs as a function of  $CAPE$  ( $m^2 s^{-2}$ ) and  $Q_{Ra}$  ( $Q_{Ra}$  symbolizes the total volumetric amount of  
 164 cloud ice, graupel, and snow in the charge separation region) as

$$165 f_l = \alpha_l Q_{Ra} CAPE^{1.3} \quad (5)$$

$$166 f_o = \alpha_o Q_{Ra} CAPE^{1.3} \quad (6)$$

167 where  $f_l$  and  $f_o$  respectively symbolize the total flash density ( $fl. m^{-2} s^{-1}$ ) over land and ocean. In addition,  $\alpha_l$  and  $\alpha_o$  are  
 168 constants ( $fl. s^{1.6} kg^{-1} m^{-2.6}$ ) determined after calibration against LIS/OTD climatology, respectively, for land and ocean.  
 169 For this study,  $\alpha_l$  and  $\alpha_o$  are set respectively as  $2.67 \times 10^{-16}$  and  $1.68 \times 10^{-17}$ . In the charge separation region (from  $0^\circ$  to  
 170  $-25^\circ C$  isotherm),  $Q_{Ra}$  ( $kg m^{-2}$ ) is expressed as a proxy for the charging rate because of collisions between graupel and  
 171 hydrometeors of other types (McCaul et al., 2009). Moreover,  $Q_{Ra}$  represents the total volumetric amount of hydrometeors of  
 172 three kinds (graupel, snow, and cloud ice) within the charge separation region, calculated as

$$173 Q_{Ra} = \int_{z_0}^{z-25} (q_{graup} + q_{snow} + q_{ice}) \bar{\rho} dz, \quad (7)$$

174 where  $q_{graup}$ ,  $q_{snow}$ , and  $q_{ice}$  respectively represent the mass mixing ratios ( $kg kg^{-1}$ ) of graupel, snow, and cloud ice. In  
 175 addition,  $q_{ice}$  was diagnosed using Arakawa–Schubert cumulus parameterization. Then,  $q_{graup}$  and  $q_{snow}$  were computed at  
 176 each vertical level of the model using the following equations.

$$177 q_{graup} = \beta \frac{P_f}{\bar{\rho} V_{graup}} \quad (8)$$

$$178 q_{snow} = (1 - \beta) \frac{P_f}{\bar{\rho} V_{snow}} \quad (9)$$

179 In those equations,  $P_f$  represents the vertical profile of the frozen precipitation convective flux ( $kg m^{-2} s^{-1}$ ),  $\bar{\rho}$  denotes the  
 180 air density ( $kg m^{-3}$ ), and  $V_{graup}$  and  $V_{snow}$  respectively express the typical fall speeds for graupel and snow set to 3.1 and 0.5  
 181  $m s^{-1}$  for this study. For land, the dimensionless coefficient  $\beta$  is set as 0.7, whereas it is set to 0.45 for oceans to consider  
 182 the observed lower graupel content over the oceans.

183

184 Based on the cold cloud depth, a fourth-order polynomial (equation 10) is used to calculate the proportion of total flashes  
 185 that are cloud-to-ground ( $p$ ). An earlier report of the literature describes the method (Price and Rind, 1993).

$$186 p = \frac{1}{64.9 - 36.54D + 7.493D^2 - 0.648D^3 + 0.021D^4} \quad (10)$$

187 The depth of the cloud above the  $0^\circ C$  isotherms is represented by  $D$  (km) in that equation.

188

189 According to recent studies, the intra-cloud (IC) lightning flashes are as efficient as cloud-to-ground (CG) lightning flashes  
 190 at producing  $NO_x$ . The lightning  $NO_x$  production efficiency is estimated as 100–400 mol per flash (Ridley et al., 2005;  
 191 Cooray et al., 2009; Ott et al., 2010; Allen et al., 2019). The  $LNO_x$  production efficiencies for IC and CG are therefore set to  
 192 the same value (250 mol per flash) in CHASER, which is the median of the commonly cited range of 100–400 mol per flash.

193 Therefore, in this study, the distinctions between IC and CG do not affect the distribution or magnitude of LNO<sub>x</sub> emissions.  
194 It is noteworthy that marked uncertainties are involved in ascertaining the LNO<sub>x</sub> production efficiency (Allen et al., 2019;  
195 Bucselo et al., 2019). The choice of a different LNO<sub>x</sub> production efficiency might affect the simulation of LNO<sub>x</sub> emissions.  
196 Further research must be undertaken to implement and validate a more sophisticated parameterization of LNO<sub>x</sub> production  
197 efficiency in chemistry–climate models. The calculated total column LNO<sub>x</sub> for each grid was distributed into each model  
198 layer based on a prescribed “backward C-shaped” LNO<sub>x</sub> vertical profile (Ott et al., 2010).

### 199 **2.3 Lightning observation data for model evaluation**

200 We used LIS/OTD gridded climatology datasets for this study, consisting of climatologies of total LFRs observed using the  
201 Lightning Imaging Sensor (LIS) and Optical Transient Detector (OTD). The OTD aboard the MicroLab-1 satellite and LIS  
202 aboard the Tropical Rainfall Measuring Mission (TRMM) satellite (Cecil et al., 2014). Both sensors detected lightning by  
203 monitoring pulses of illumination produced by lightning in the 777.4 nm atomic oxygen multiplet above background levels.  
204 In low Earth orbit, both sensors viewed Earth locations for approximately 3 min during the pass of the OTD or 1.5 min  
205 during passing of the LIS. Each day, OTD and LIS respectively orbited the globe 14 times and 16 times. OTD observed data  
206 between +75 and -75° latitude during May 1995 – March 2000, whereas LIS collected data between +38 and -38° latitude  
207 during January 1998 – April 2015. This study uses the LIS/OTD 2.5 Degree Low Resolution Time Series (LRTS), which  
208 provides daily LFRs on a 2.5° regular latitude–longitude grid for May 1995 – April 2015.

### 209 **2.4 CMIP6 model outputs for model comparison**

210 For the comparison of different model outputs from our study (CHASER) and other Earth system models or chemistry–  
211 climate models, we used LFR and surface temperature data from the CMIP6 CMIP Historical experiments from CESM2-  
212 WACCM (Danabasoglu, 2019), GISS-E2-1-G (Kelley et al., 2020), and UKESM1-0-LL (Tang et al., 2019). CESM2-  
213 WACCM uses the Community Earth System Model ver. 2 (Danabasoglu et al., 2020). The CESM2 is an open-source fully  
214 coupled Earth system model. The Whole Atmosphere Community Climate Model ver. 6 (WACCM6) is the atmospheric  
215 component coupled to the other components in CESM2. The GISS-E2-1-G is the NASA Goddard Institute for Space Studies  
216 (GISS) chemistry–climate model version E2.1 based on the GISS Ocean v1 (G01) model (Miller et al., 2014; Kelley et al.,  
217 2020). The UKESM1-0-LL is the UK's Earth system model, details of which were described by Sellar et al. (2019). We used  
218 3 ensembles from CESM2-WACCM, 9 ensembles from GISS-E2-1-G, and 18 ensembles from UKESM1-0-LL. Table S1  
219 presents all the ensemble members used for this study.

### 220 **2.5 Experiment setup**

221 We have conducted six sets of experiments with each set of experiments conducted using both the ECMWF-McCAUL  
222 (abbreviated as F1) and CTH (abbreviated as F2) schemes. Table 1 presents the major settings of all experiments with the  
223 relative explanations of those settings. STD-F1/F2 are standard experiments with the simulation period of 1959–2014. They

224 are intended to reproduce the historical trends of lightning and LNO<sub>x</sub>. Climate1959-F1/F2 are experiments that keep the  
 225 climate simulations fixed to 1959 to derive the effects of global warming on historical lightning trends. ClimateAero1959-  
 226 F1/F2 are intended to reflect the conditions with climate simulations and aerosol and aerosol precursor (BC, OC, NO<sub>x</sub>, SO<sub>2</sub>)  
 227 emissions fixed to 1959. The Aero1959-F1/F2 experiments are the same as the STD-F1/F2 experiments, except for the  
 228 AeroPEs fixed to 1959. The fifth set of experiments (Volca-off-F1/F2) was intended to exclude the influences of the  
 229 Pinatubo volcanic eruption to compare to the STD-F1/F2 and to evaluate the Pinatubo eruption effects on historical  
 230 lightning–LNO<sub>x</sub> trends and variation.

231

232 We simulate volcanic aerosol forcing by considering the prescribed stratospheric aerosol extinction in the radiation scheme.  
 233 We used the NASA Goddard Institute for Space Studies (GISS) (Sato et al., 1993) and Chemistry–Climate Model Initiative  
 234 (CCMI) (Arfeuille et al., 2013) stratospheric aerosol dataset as the stratospheric aerosol climate data. The NASA GISS  
 235 dataset includes monthly zonal-mean stratospheric aerosol optical thickness in four spectral bands. The CCMI dataset for  
 236 CHASER includes monthly zonal-mean stratospheric aerosol extinction coefficients in 20 spectral bands. To remove the  
 237 volcanic perturbation while maintaining the stratospheric background aerosol in the Volca-off-F1/F2, we used the following  
 238 equation to process the Stratospheric Aerosol Climatology (SAC) during June 1991 – May 1996.

$$239 \quad \mathbf{SAC}_{no\_pinatubo} = \begin{cases} \mathbf{SAC}_{background}, & |\mathbf{SAC}_{raw} - \mathbf{SAC}_{background}| > 1.96\sigma, \\ \mathbf{SAC}_{raw}, & |\mathbf{SAC}_{raw} - \mathbf{SAC}_{background}| \leq 1.96\sigma \end{cases} \quad (11)$$

240 In that equation,  $\mathbf{SAC}_{no\_pinatubo}$  denotes the stratospheric aerosol climatological data as input data for Volca-off-F1/F2  
 241 experiments,  $\mathbf{SAC}_{background}$  represents the stratospheric background aerosol climatological data (For this study,  
 242  $\mathbf{SAC}_{background}$  is the corresponding temporal averaged values of the NASA GISS and CCMI stratospheric aerosol  
 243 dataset during June 1986 – May 1991 and June 1996 – May 2001, when the time is close to the eruption and the  
 244 stratosphere was less affected by volcanic eruptions).  $\mathbf{SAC}_{raw}$  stands for the original values of NASA GISS and CCMI  
 245 stratospheric aerosol dataset during June 1991 – May 1996. Moreover,  $\sigma$  symbolizes the standard deviations of  
 246 stratospheric background aerosol climate data (For this study,  $\sigma$  are the corresponding standard deviations of NASA  
 247 GISS and CCMI stratospheric aerosol dataset during June 1986 – May 1991 and June 1996 – May 2001). As displayed  
 248 in Eq. (11), when the absolute differences between  $\mathbf{SAC}_{raw}$  and  $\mathbf{SAC}_{background}$  are larger than  $1.96\sigma$ , we replace the  
 249 original values (June 1991 – May 1996) of the SAC with the temporal averaged values of the NASA GISS and CCMI  
 250 dataset during June 1986 – May 1991 and June 1996 – May 2001. When the absolute differences between  $\mathbf{SAC}_{raw}$  and  
 251  $\mathbf{SAC}_{background}$  are equal to or smaller than  $1.96\sigma$ , we still use the original values (June 1991 – May 1996) of the SAC  
 252 for the Volca-off experiments. The value of  $1.96\sigma$  corresponds to the 95% confidence interval, which can remove the  
 253 Pinatubo perturbation sufficiently but which can maintain the background level of stratospheric aerosol during June  
 254 1991 – May 1996. Furthermore, the influences of the Pinatubo eruption affected the HadISST SSTs/sea ice fields. To



255 remove the Pinatubo eruption's influences on the SSTs/sea ice fields from the Volca-off experiments also, we replaced  
 256 the 1991-06 – 1995-05 SSTs/sea ice data with HadISST SSTs/sea ice climatological data during 1985–1990 when  
 257 conducting the Volca-off experiments. The 1985–1990 period was chosen because it is approximately the period of  
 258 1991-06 – 1995-05 and because the SSTs/sea ice fields were less affected by volcanic activity during 1985–1990.

259

260 All the experiments calculate the LNO<sub>x</sub> emissions rates interactively by LNO<sub>x</sub> emission parameterizations except STD-  
 261 rVolcaoff experiments. The STD-rVolcaoff experiments are the same as the STD experiments except for reading the  
 262 daily LNO<sub>x</sub> emission rates calculated from the Volca-off experiments. The STD-rVolcaoff experiments are conducted  
 263 for comparison with STD experiments to elucidate the effects of LNO<sub>x</sub> emissions changes caused by the Pinatubo  
 264 eruption on atmospheric chemistry (typically methane lifetime).

265

**Table 1: All experiments conducted for this study**

| Name of experiment     | Period    | Climate (SSTs, sea ice, GHGs) <sup>a</sup>   | Anthropogenic and biomass burning emissions | Biogenic emissions           | Stratospheric aerosol climatology                             |
|------------------------|-----------|--|---|------------------------------|---|
| STD-F1/F2 <sup>b</sup> | 1959–2014 | 1959–2014  | CMIP6 1959–2014                             |                              | NASA GISS and CCM1 stratospheric aerosol dataset <sup>c</sup> |
| Climate1959-F1/F2      | 1959–2014 | Fixed to 1959 <sup>d</sup>   | CMIP6 1959–2014                             | VISIT and MEGAN <sup>f</sup> | As above  |
| ClimateAero1959-F1/F2  | 1959–2014 | Fixed to 1959  | AeroPEs fixed to 1959 <sup>e</sup>          |                              | As above  |
| Aero1959-F1/F2         | 1959–2014 | 1959–2014  | AeroPEs fixed to 1959                       |                              | As above  |
| Volca-off-F1/F2        | 1990–1999 | 1990–1999 <sup>g</sup>   | CMIP6 1990–1999                             |                              | Same dataset with volcanic perturbation removed               |
| STD-rVolcaoff-F1/F2    | 1990–1999 | All settings are the same as those used for STD experiment except for reading of the daily LNO <sub>x</sub> emission rates calculated from the Volca-off experiments |   |                              |   |

266 <sup>a</sup> For the model simulations, the climate is simulated by the prescribed SSTs/sea ice fields and the prescribed varying  
 267 concentrations of GHGs (CO<sub>2</sub>, N<sub>2</sub>O, methane, chlorofluorocarbons – CFCs – and hydrochlorofluorocarbons – HCFCs) used  
 268 only in the radiation scheme. The SSTs/sea ice fields are obtained from the HadISST dataset (Rayner et al., 2003). The  
 269 prescribed GHGs concentrations are derived from CMIP6 forcing datasets (Meinshausen et al., 2017).

270 <sup>b</sup> We use “F1” to stand for the ECMWF-McCAUL scheme; “F2” represents the CTH scheme.

271 <sup>c</sup> Stratospheric aerosol radiative forcing is simulated using the prescribed stratospheric aerosol extinction, which is obtained  
272 from the NASA GISS (Sato et al., 1993) and CCMI (Arfeuille et al., 2013) stratospheric aerosol dataset.

273 <sup>d</sup> The climate is fixed to 1959 for the whole simulation period using the 1959 SSTs/sea ice field and GHG concentrations  
274 during the simulation period.

275 <sup>e</sup> Aerosol (BC, OC) and aerosol precursor (NO<sub>x</sub>, SO<sub>2</sub>) emissions (anthropogenic + biomass burning) are fixed to 1959  
276 throughout the simulation period.

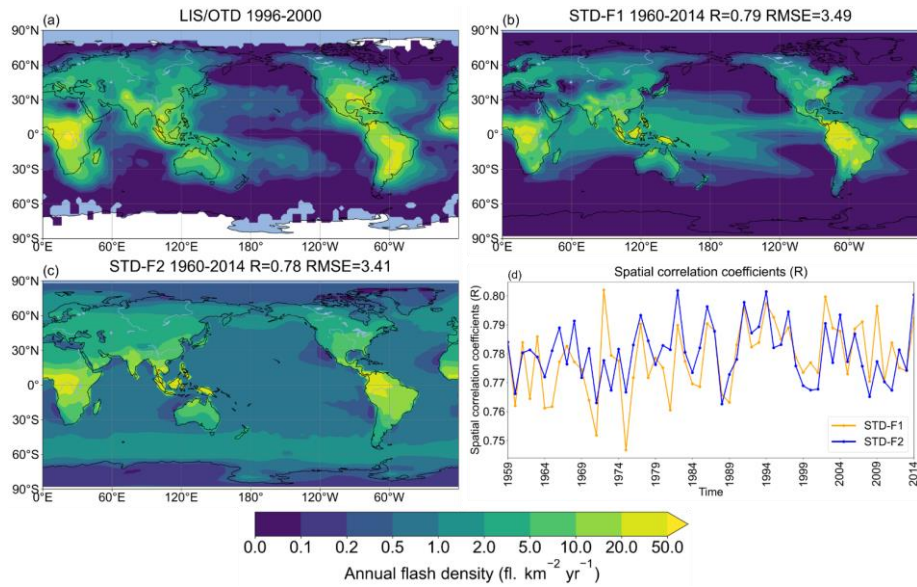
277 <sup>f</sup> Several biogenic emissions are interannually varying, including isoprene, monoterpenes, acetone, and methanol, which  
278 were calculated using an off-line simulation using the Vegetation Integrative Simulator for Trace Gases (VISIT) terrestrial  
279 ecosystem model (Ito and Inatomi, 2012). Some other reactive biogenic VOCs (ethane, propane, ethylene, propene) used are  
280 climatological data derived from the Model of Emissions of Gases and Aerosols from Nature (MEGAN) modeling system  
281 (Guenther et al., 2012).

282 <sup>g</sup> Here the 1991-06 – 1995-05 SSTs/sea ice data were replaced with HadISST SSTs/sea ice climatological data during  
283 1985–1990.

## 284 **3 Results and Discussion**

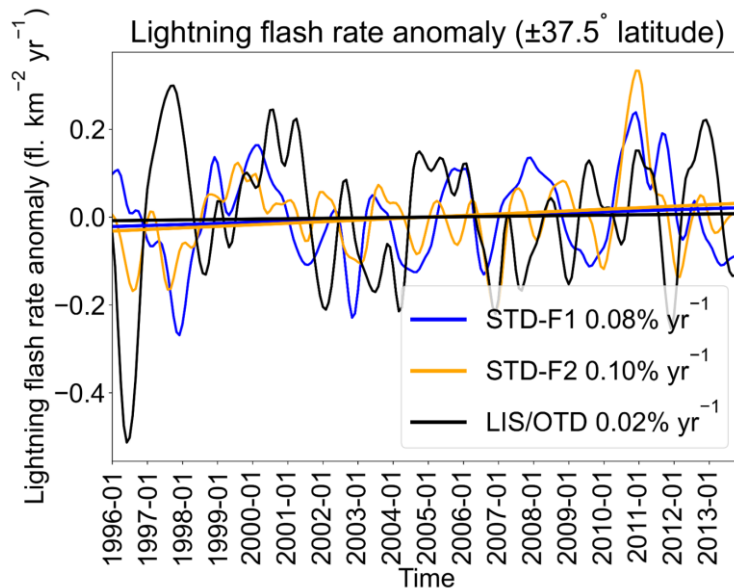
### 285 **3.1 Validation of the simulated historical lightning distribution and trend**

286 To increase the credibility of the conclusions obtained based only on the numerical simulations, the model calculations must  
287 be evaluated using observational data. We used the LIS/OTD observations to evaluate the spatial and temporal distribution  
288 and historical lightning trends simulated by CHASER (MIROC). Figures 1a–1c show the annual mean spatial distributions  
289 of lightning observed by LIS/OTD and from model simulations using the ECMWF-McCAUL and CTH schemes. Both the  
290 ECMWF-McCAUL and CTH schemes generally captured the hotspots of lightning (Central Africa, Maritime Continent,  
291 South America), with strong spatial correlations between observations and model simulations ( $R > 0.75$ ). Figure 1d exhibits  
292 strong spatial correlation between observations and simulation results maintained throughout the simulation period (1959–  
293 2014).



294

295 **Figure 1: Annual mean lightning flash densities from (a) LIS/OTD satellite observations spanning 1996–2000, (b) the**  
 296 **STD experiment (1960–2014) with the ECMWF-McCAUL scheme used, (c) the STD experiment (1960–2014) with the CTH scheme**  
 297 **used.  $R$  and RMSE shown in the titles of panels (b) and (c) are calculated between panels (b)–(c) and (a). Panel (d) presents the**  
 298 **spatial correlation coefficients between modeled spatial lightning distribution of each year and LIS/OTD lightning climatologies**  
 299 **during 1996–2000.**



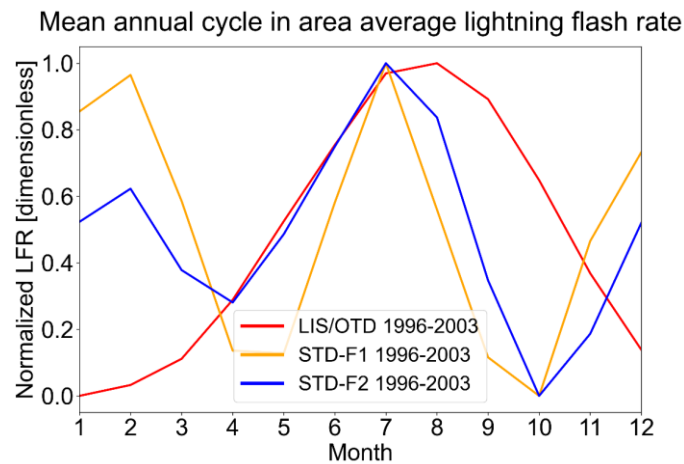
300

301 **Figure 2: LFR anomalies of 1996–2013 within  $\pm 37.5^\circ$  latitude obtained from two numerical experiments (STD-F1/F2) and**  
 302 **LIS/OTD satellite observations. Curves represent the monthly time-series data of the  $\pm 37.5^\circ$  latitude mean LFR anomalies with the**

303 **1-D Gaussian (Denoising) filter applied. Lines are the fitting curves of the monthly time-series data of the  $\pm 37.5^\circ$  latitude mean**  
304 **LFR anomalies. Trends of the LFR anomalies in  $\% \text{ yr}^{-1}$  are also presented in the legends.**

305

306 The LIS/OTD observations are also used to evaluate historical lightning trends simulated by CHASER (MIROC). We  
307 examined the  $\pm 37.5^\circ$  latitude mean LFR anomaly (1996–2013) calculated from LIS/OTD observations and STD-F1/F2  
308 numerical experiments (Fig. 2). We also note some missing values within the  $\pm 37.5^\circ$  latitude in LIS/OTD observations. To  
309 constrain the comparisons between observations and simulations as like-for-like, when we encounter a missing value in the  
310 LIS/OTD observations during spatial averaging, we also treat the CHASER simulated value at the same location as a  
311 missing value. As displayed in Fig. 2, even when the interannual variations of the LFR anomaly sometimes differ between  
312 observations and simulations, the overall trends of LFR anomaly simulated using both schemes well-matched the LIS/OTD  
313 observations. Neither the LFR anomaly (within  $\pm 37.5^\circ$  latitude) derived from LIS/OTD observations nor simulations show a  
314 significant trend for 1996–2013 using the Mann–Kendall rank statistic test (significance inferred for 5%). The global LFR  
315 anomaly during 1993–2013 obtained from simulations (STD-F1/F2) also shows no significant trend, which is consistent with  
316 the Schuman Resonance (SR) intensity observations (1993–2013) at Rhode Island, USA (Earle Williams, 2022). However,  
317 the SR observations in Rhode Island (USA) exclude consideration of the influences of solar cycles, which makes it less  
318 appropriate for lightning trend evaluation.



319

320 **Figure 3: Mean annual cycle in area average LFR during 1996–2003. The area average was taken over the grid cells where valid**  
321 **LIS/OTD lightning observations exist. LFR is normalized by min-max normalization.**

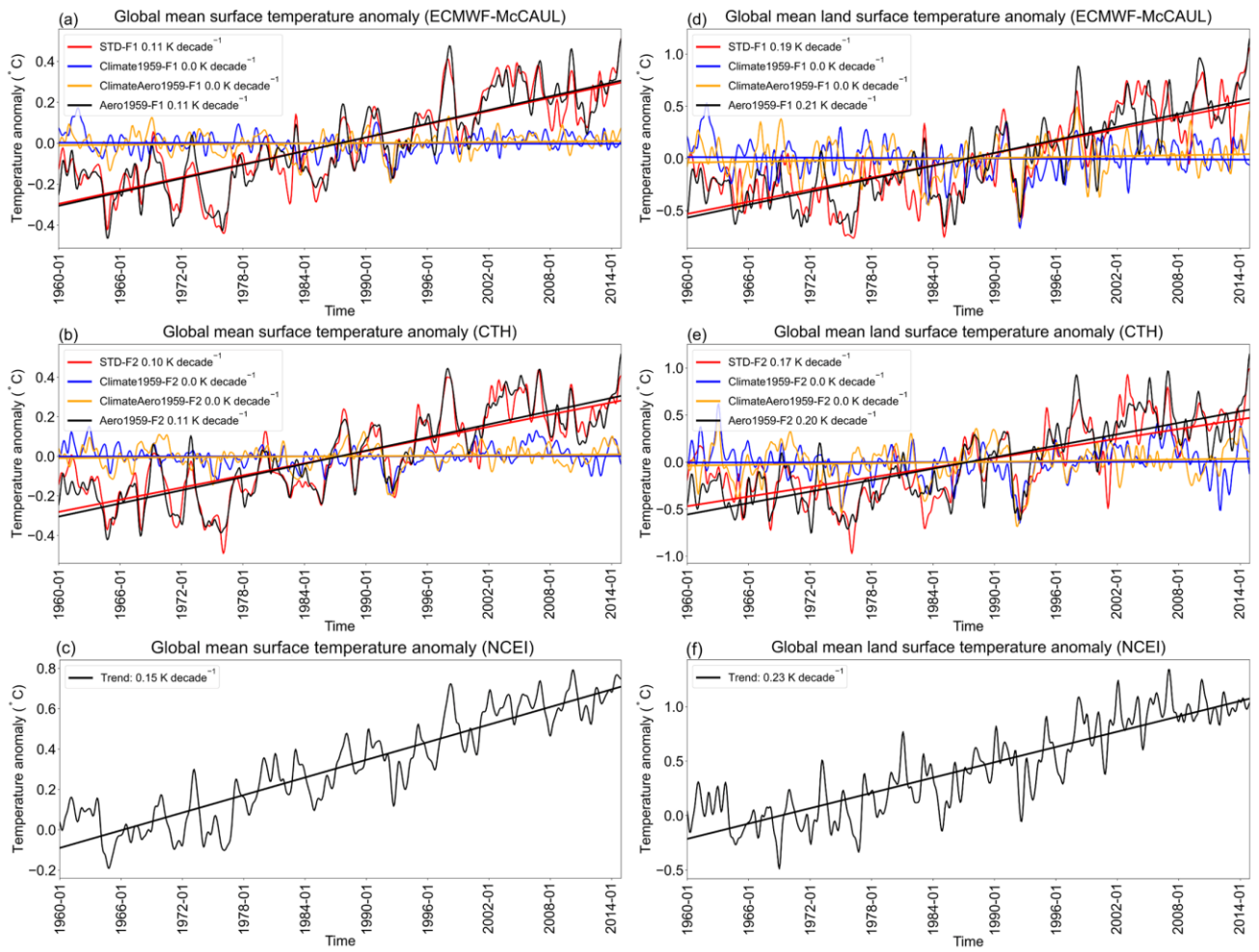
322

323 We further investigated the seasonal variabilities of simulated LFR and compared them against LIS/OTD observations. The  
324 results are depicted in Fig. 3. Both the CTH and ECMWF-McCAUL schemes captured the peak during JJA, but the  
325 overestimation of LFR by F1/F2 during DJF is also noticeable. Figure S1 presents comparison of the LFR global distribution  
326 in different seasons during 1996–2003 from LIS/OTD lightning observations and STD experiment outputs. Generally,  
327 CHASER well-captured the spatial distribution of LFR in all four seasons when compared against LIS/OTD observations.

328 The spatial correlation coefficients ( $R$ ) between observations and simulations are highest ( $R=0.80$  for both lightning  
329 schemes) in DJF, indicating CHASER's considerable capability to reproduce the LFR spatial distribution in DJF. As  
330 displayed in the first row of Fig. S1, the overestimation of LFR by F1/F2 during DJF is primarily attributable to the  
331 overestimation of LFR within the Maritime Continent and South America, but this might also be attributable to the  
332 underestimation of LFR by LIS/OTD within these two regions. It is believed that the LIS/OTD lightning detection efficiency  
333 is highly sensitive to the characteristic of convective clouds (cloud albedo, cloud optical thickness, etc.) (Boccippio et al.,  
334 2002; Cecil et al., 2014). High cloud albedo and cloud optical thickness might engender the underestimation of LFR by  
335 LIS/OTD. It is also noteworthy that the seasonal variation and long-term trend of global lightning are strongly influenced by  
336 distinct different factors. The seasonal variation of global lightning activities is most strongly affected by the  $23^\circ$  obliquity of  
337 Earth's orbit and the asymmetric distribution of the continent between the Northern and Southern hemispheres. However, the  
338 long-term global lightning trend we investigated for this study is controlled mainly by climate forcers such as aerosols and  
339 GHGs. To minimize the effects of LFR seasonal variation on our study's results, we deseasonalized the results shown in all  
340 figures and tables by calculating their anomaly based on raw data. The validation described above and the deseasonalization  
341 of our study's results justified that the LFR seasonal variation (and the uncertainties in the simulation of LFR seasonal  
342 variation) in our study has a limited effect on these study results.

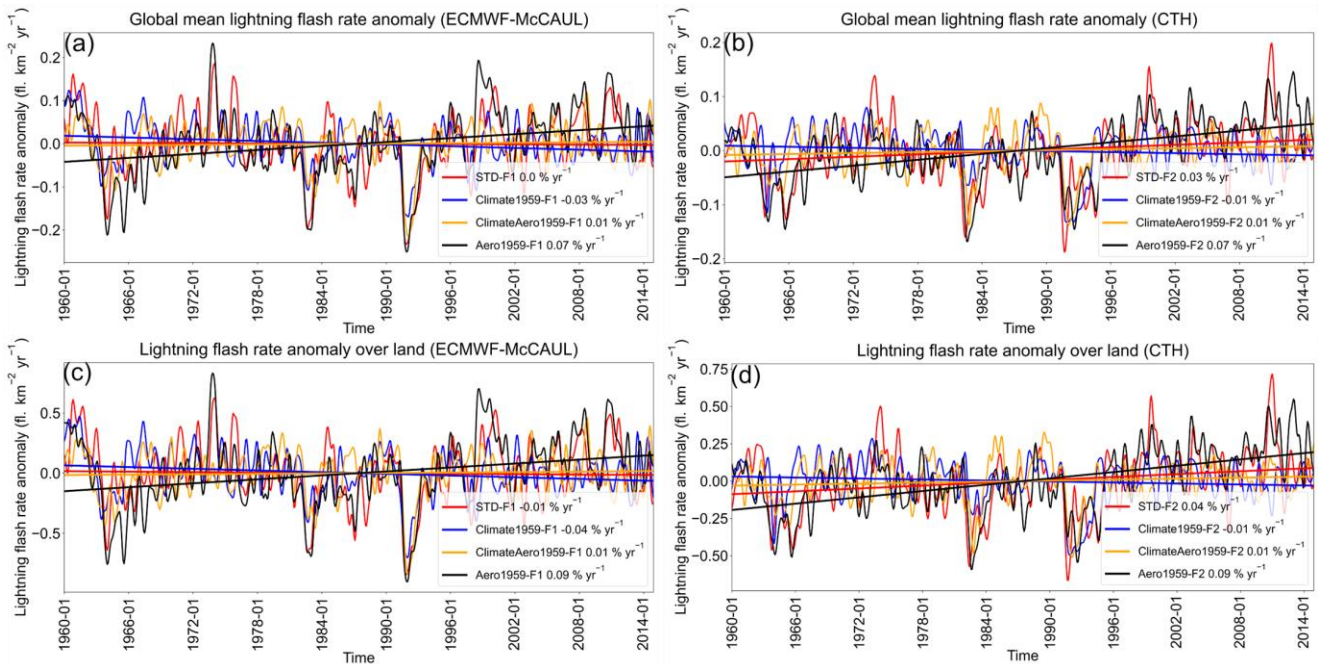
### 343 **3.2 Effects of global warming and increases in AeroPEs on historical lightning–LNO<sub>x</sub> trends**

344 As introduced in Sect. 1, global warming and changes in AeroPEs are the two main factors which influence long-term  
345 (1960–2014) historical lightning trends (Hereinafter, historical lightning trends represent lightning trends of 1960–2014.). To  
346 analyze the effects of global warming on historical lightning trends, we designed and conducted two sets of experiments: one  
347 set of experiments including “global warming” (STD-F1/F2) and another set of experiments excluding “global warming”  
348 (Climate1959-F1/F2). Figures 4a and 4b respectively depict the global surface temperature anomalies calculated using the  
349 ECMWF-McCAUL and CTH schemes. The STD and Aero1959 experiments show an increasing trend (around 0.11 K  
350 decade<sup>-1</sup>) of global mean surface temperature anomalies, which closely approximates the trend (around 0.15 K decade<sup>-1</sup>)  
351 obtained from NOAA's National Centers for Environmental Information (NCEI) (Figs. 4c, 4f). Global temperature change  
352 data from 1880 to the present are available from the NCEI, which tracks variations of the Earth's temperature based on  
353 thousands of stations' observation data around the globe (Climate at a Glance | National Centers for Environmental  
354 Information (NCEI), 2022). When the prescribed SSTs/sea ice fields and GHGs concentrations were fixed to 1959  
355 throughout the simulation period, the simulated trends of global mean surface temperature anomalies turned out to be flat  
356 (Climate1959 and ClimateAero1959). To elucidate the effects of increases in AeroPEs on averaged surface temperature to  
357 the greatest extent possible, we also show the averaged surface temperature anomaly only over land regions (Figs. 4d–4f).  
358 The simulated global mean land surface temperature anomalies are also well-matched with the NCEI observational data. The  
359 aerosol cooling effect can be more evident when only examining surface temperature trends averaged over land (Figs. 4d–  
360 4e).



361

362 **Figure 4: Monthly time-series data of global mean surface temperature anomalies with 1-D Gaussian (Denosing) filter applied and**  
 363 **their fitting curves calculated from the outputs of numerical experiments (a–b) and obtained from NCEI (c). Panels (d)–(f) are the**  
 364 **same as panels (a)–(c), but the averaged surface temperature anomalies are only calculated within the global land regions. The**  
 365 **trends of the fitting curves in K decade<sup>-1</sup> are also presented in the legends.**



366

367 **Figure 5: Panels (a) and (b) show monthly time-series data of global mean LFR anomalies with 1-D Gaussian (Denosing) Filter**  
 368 **applied and their fitting curves of different experiments simulated respectively using the ECMWF-McCAUL scheme and CTH**  
 369 **scheme. Panels (c) and (d) are the same as panels (a) and (b), except that the averaged LFR anomalies are calculated only within**  
 370 **global land regions. Trends of the fitting curves ( $\% \text{ yr}^{-1}$ ) are also shown in the legends.**

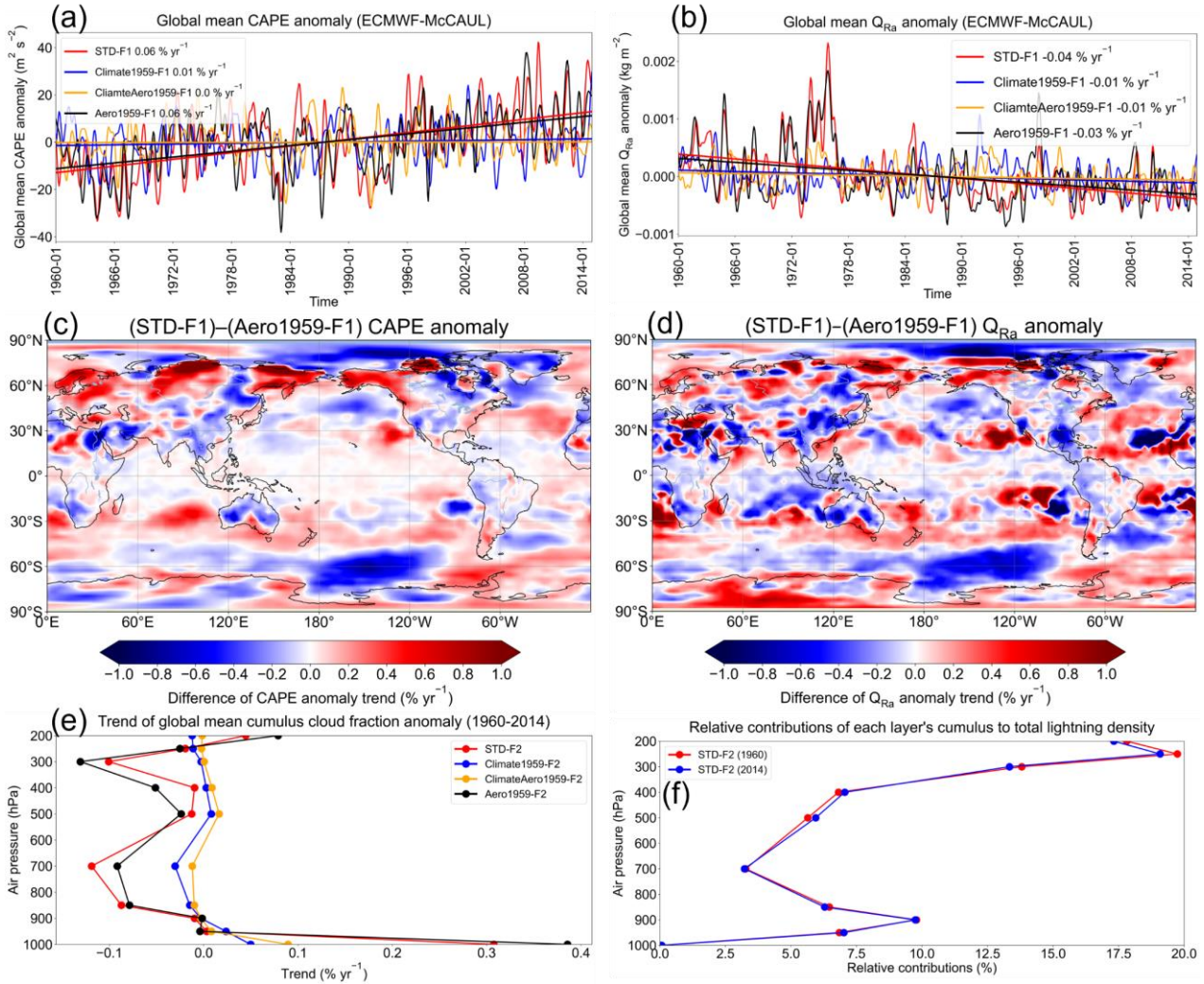
371

372 Figure 5, panels (a) and (b) respectively portray the global mean LFR anomalies and their fitting curves obtained from the  
 373 outputs of the ECMWF-McCAUL scheme and CTH scheme. The global lightning trend obtained from the STD-F1  
 374 experiment turned out to be statistically flat ( $0.0\% \text{ yr}^{-1}$ ), whereas the outputs of the STD-F2 experiment exhibit a not  
 375 significant increasing global lightning trend ( $0.03\% \text{ yr}^{-1}$ ) determined using the Mann–Kendall rank statistic (significance  
 376 inferred for 5%).

377

378 Comparison of the lightning trends calculated from the STD and Climate1959 experiments showed that both lightning  
 379 schemes demonstrated that historical global warming (1960–2014) enhances the global lightning trends toward positive  
 380 trends (around  $0.03\% \text{ yr}^{-1}$  or  $3\% \text{ K}^{-1}$ ). Global warming effects on historical lightning trends were evaluated as significant  
 381 using the Mann–Kendall rank statistic, with significance inferred for 5%, when using the CTH scheme, but not in the case of  
 382 the ECMWF-McCAUL scheme (Hussain and Mahmud, 2019). The differences in lightning trends simulated by the STD-  
 383 F1/F2 and Aero1959-F1/F2 experiments indicate that the increases in AeroPEs during 1960–2014 significantly suppress the  
 384 global lightning trends ( $-0.07\% \text{ yr}^{-1}$  –  $-0.04\% \text{ yr}^{-1}$ ). It is noteworthy that this suppression of lightning trends is only  
 385 attributable to aerosol radiative effects. Further research must be conducted to elucidate the long-term effects of aerosols on  
 386 lightning through aerosol microphysical effects. We also investigated lightning trends only over land regions (Figs. 5c–5d) to

387 ascertain the effects of changes in AeroPEs to the greatest extent possible. When observing the lightning trends over land  
 388 only, the degree of suppression of lightning trends attributable to increases in AeroPEs expands to  $-0.10\% \text{ yr}^{-1} - -0.05\% \text{ yr}^{-1}$ ,  
 389 which is attributable to most AeroPEs and their growth coming from land regions. It is noteworthy that we used the same  
 390 SSTs/sea ice data in the Aero1959 as those used for STD experiments. The SSTs/sea ice data also reflected the effects of  
 391 increases in AeroPEs. Therefore, we might underestimate the effects of increases in AeroPEs on lightning trends by  
 392 comparing the results of STD and Aero1959 experiments.



393  
 394 **Figure 6:** Panels (a) and (b) respectively show monthly time-series data of global mean CAPE and  $Q_{Ra}$  anomalies with 1-D  
 395 Gaussian (Denoising) filter applied and their fitting curves simulated using the ECMWF-McCAUL scheme. Panels (c) and (d)  
 396 respectively show differences in the CAPE anomaly trend and  $Q_{Ra}$  anomaly trend of the STD-F1 and Aero1959-F1 experiments in  
 397 the global map. Figure 6(e) portrays the vertical profiles of the trend of global mean cumulus cloud fraction anomaly simulated by

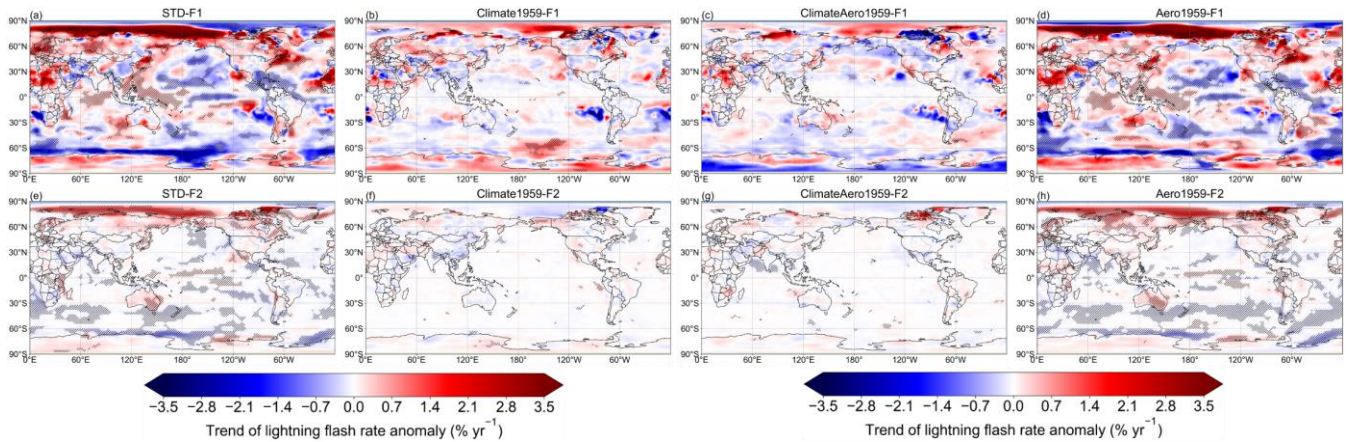


398 **the CTH scheme. Panel (f) depicts the relative contributions of each layer’s cumulus to total lightning density in 1960 and 2014, as**  
399 **calculated from the outputs of the STD-F2 experiment.**

400

401 For the ECMWF-McCAUL scheme, model outputs affirm that global warming can enhance the global mean CAPE anomaly  
402 slightly and suppress the global mean  $Q_{Ra}$  anomaly (Figs. 6a–6b). Earlier studies have also indicated that the total solid  
403 (cloud ice, snow, and graupel) mass mixing ratio within charge separation regions is lower under global warming. Moreover,  
404 possible explanations are given in those studies (Finney et al., 2018; Romps, 2019). Because global warming enhances  
405 global convection activities, and because lightning formation is highly related to convection activity, global warming  
406 enhances the historical global lightning trend simulated using the ECMWF-McCAUL scheme, mainly as a result of the  
407 simulated CAPE trend, which is enhanced by global warming. The past increases in AeroPEs exert negligible effects on the  
408 trends of global mean CAPE and  $Q_{Ra}$  anomalies, as displayed in Figs. 6a–6b. However, the past increases in AeroPEs  
409 suppress the CAPE and  $Q_{Ra}$  trend within the tropical and subtropical terrestrial regions, where lightning densities are high  
410 (Figs. 6c–6d). Weaker convection activities (smaller CAPE) and fewer hydrometeors (cloud ice, graupel, snow) in the charge  
411 separation regions ( $0^{\circ}\text{C} - -25^{\circ}\text{C}$  isotherm) engender less lightning. These are the main causes for the suppression of the  
412 historical lightning trends induced by increases in AeroPEs through aerosol radiative effects. It is noteworthy that, because  
413 the aerosol microphysical effects are only considered in the grid-scale large-scale condensation scheme, our study might  
414 underestimate the aerosol microphysical effects which can enhance the trends of  $Q_{Ra}$  and LFR toward the positive direction.  
415

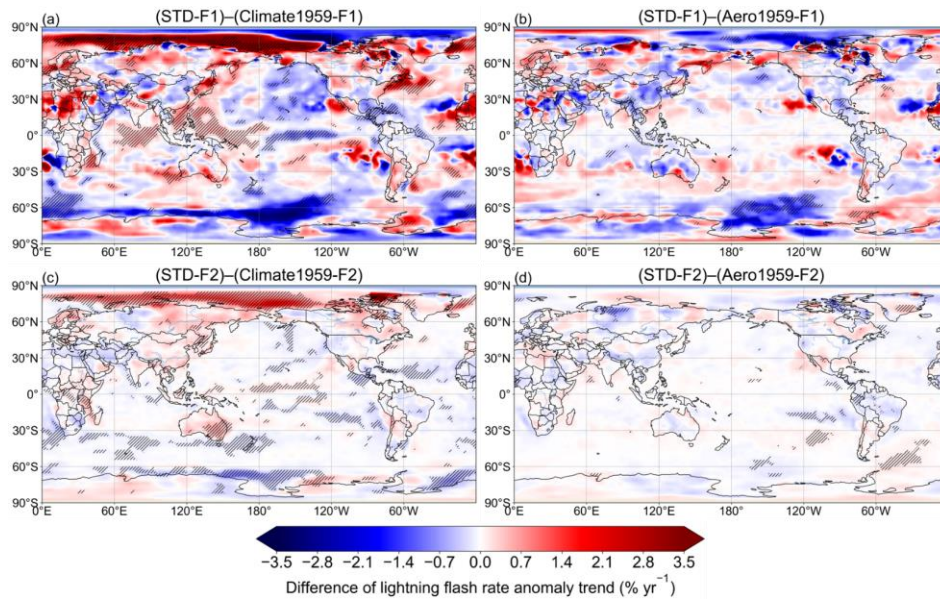
416 To explain the results simulated by the CTH scheme, we investigated the vertical profiles of the trend of the global mean  
417 cumulus cloud fraction anomaly (Fig. 6e). Investigating cumulus cloud fraction is reasonable because each model layer’s  
418 cumulus cloud fractions are used to weight the calculated lightning densities from that layer in the CTH scheme, as  
419 introduced in equations (3) and (4). Figure 6f shows the relative contributions of each model layer’s cumulus to the  
420 calculated global total lightning densities in 1960 and 2014 obtained using the CTH scheme. As Fig. 6f displayed, the  
421 vertical profiles of relative contribution in 1960 and 2014 are almost identical. Cumulus convection is positively correlated  
422 with lightning formation, which is the scientific basis of parameterizing lightning densities using the cumulus cloud top  
423 height: the CTH scheme. Historical global warming enhances the lightning trend simulated by the CTH scheme mainly  
424 because the simulated historical global warming increases the cumulus reaching 200 hPa, which contributes greatly to the  
425 simulated global total lightning density (Figs. 6e–6f). The increases in the deep convective cloud are regarded as related to  
426 the increases in tropopause height attributable to global warming, as shown in Fig. S2. The past increases in AeroPEs  
427 suppress the lightning trend simulated by the CTH scheme because increases in AeroPEs decrease the cumulus reaching 200  
428 hPa as well as the cumulus within the lower to middle troposphere by aerosol radiative effects (Fig. 6e). In addition, in the  
429 supplement, we present a figure (Fig. S3) resembling Fig. 6, but which includes only consideration of land regions. The  
430 mechanisms of global warming and increases in AeroPEs affecting lightning trends over land regions are similar to those  
431 described above on a global scale. We do not discuss details of them here.



433

434 **Figure 7: Trends of LFR anomaly ( $\% \text{ yr}^{-1}$ ) during 1960–2014 on the two-dimensional map. The trend at every point was calculated**  
 435 **from the function of approximating curve for the 1960–2014 time-series data (LFR anomaly) at each grid cell. The area in which**  
 436 **the trend was found to be significant by the Mann–Kendall rank statistic test (significance inferred for 5%) is marked with**  
 437 **hatched lines.**

438



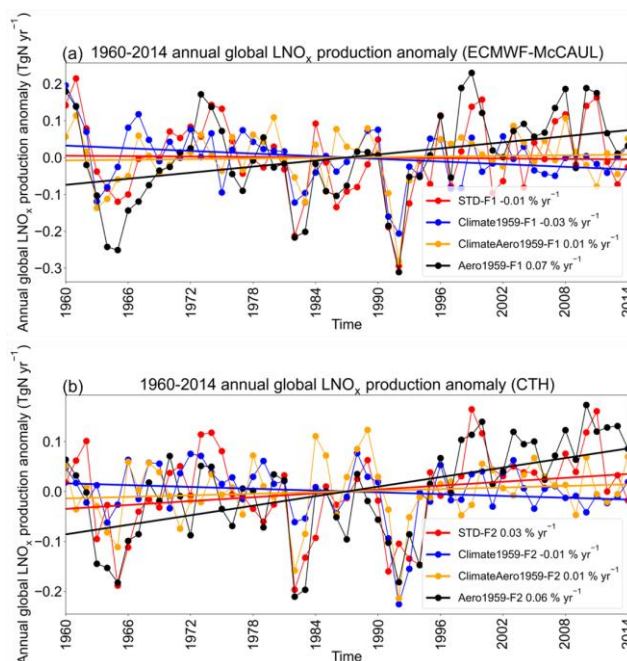
439

440 **Figure 8: Differences in trends of LFR anomaly during 1960–2014 on the global map. The area in which the trend of the**  
 441 **differences of LFR anomaly time-series data was found to be significant by the Mann–Kendall rank statistic test (significance**  
 442 **inferred for 5%) is marked with hatched lines.**

443

444 We also investigated lightning trends simulated in different experiments with the global map (Fig. 7). Both the ECMWF-  
 445 McCAUL and the CTH schemes show that lightning increased significantly in most parts of the Arctic region and decreased

446 in some parts of the Southern Ocean during 1960–2014 (Figs. 7a, 7e). The significant lightning trends presented in Figs. 7a  
 447 became nearly nonexistent when the climate simulations were fixed to 1959 (Figs. 7b, 7f), indicating the considerable effects  
 448 of global warming on the trend of global lightning activities. Furthermore, the effects of past global warming and increases  
 449 in AeroPEs on the lightning trends on the global map are displayed in Fig. 8. Figures 8a and 8c show that past global  
 450 warming enhances lightning activities within the Arctic region and Japan, which is consistent with findings of an earlier  
 451 study from which Japan thunder day data were reported (Fujibe, 2017). Figures 8a and 8c also show that historical global  
 452 warming suppresses lightning activities around New Zealand and some parts of the Southern Ocean. Both lightning schemes  
 453 demonstrated that the historical increases in AeroPEs suppress lightning activities in some parts of the Southern Ocean and  
 454 South America. The ECMWF-McCAUL scheme also suggests that historical increases in AeroPEs suppress lightning  
 455 activities by aerosol radiative effects in some parts of India and China, where AeroPEs increased dramatically during 1960–  
 456 2014 because of rapid economic development and energy consumption. Many observation-based studies indicate that  
 457 aerosols can invigorate lightning activities in some regions of China and India, typically under relatively clean conditions  
 458 (e.g.,  $\text{AOD} < 1.0$ ), which is attributable to the aerosol microphysical effects (Wang et al., 2011; Zhao et al., 2017; Lal et al.,  
 459 2018; Liu et al., 2020; Shi et al., 2020; Zhao et al., 2020). Therefore, a total positive effect of aerosol on historical lightning  
 460 trends in China and India cannot be ruled out. We further provided the same figures as Figs. 7 and 8, but using different units  
 461 ( $\text{fl. km}^{-2} \text{ yr}^{-2}$ ) in the supplementary information (Figs. S4 and S5). Figures S4 and S5 show that the absolute lightning trends  
 462 ( $\text{fl. km}^{-2} \text{ yr}^{-2}$ ) and the effects of global warming and increases in AeroPEs on the absolute lightning trends are slight in high-  
 463 latitude regions but prominent in tropical areas.



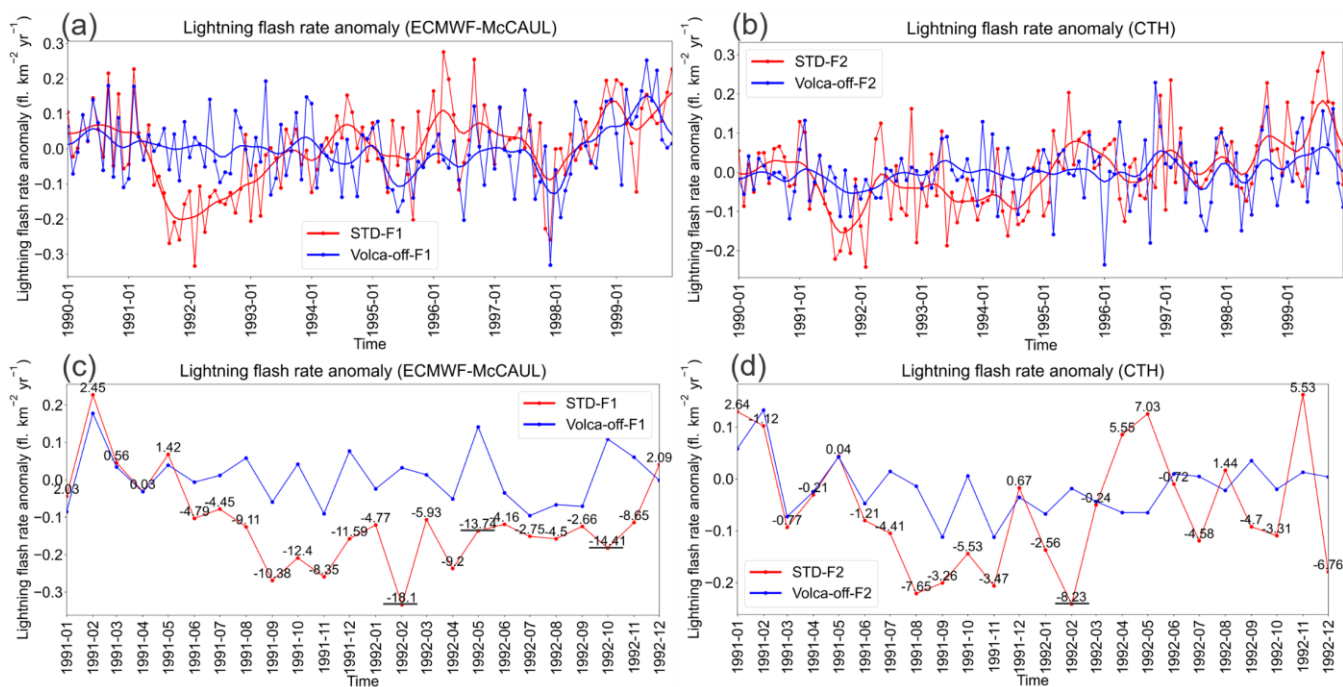
464

465 **Figure 9: Time-series data of 1960–2014 annual global LNO<sub>x</sub> production anomalies (TgN yr<sup>-1</sup>) and their fitting curves simulated**  
 466 **using the ECMWF-McCAUL scheme (a) and the CTH scheme (b). Trends of the fitting curves in percent per year are presented in**  
 467 **the legends.**

468  
 469 Trends in historical annual global LNO<sub>x</sub> emissions for different scenarios are generally consistent with trends in historical  
 470 global mean LFRs, as shown in Figs. 5a–5b and Fig. 9. This finding is not surprising because, as the lightning NO<sub>x</sub> emission  
 471 parameterizations introduced in Sect. 2.2 show, the simulated LFRs are linearly related to the simulated LNO<sub>x</sub> emissions in  
 472 our study. The results presented in Fig. 9 imply that historical global warming and increases in AeroPEs can affect  
 473 atmospheric chemistry and can engender feedback by influencing LNO<sub>x</sub> emissions.

### 474 3.3 Pinatubo volcanic eruption effects on historical lightning–LNO<sub>x</sub> trends

475 We estimate the Pinatubo eruption effects on historical lightning–LNO<sub>x</sub> trends and variation by comparing the simulation  
 476 results of STD and Volca-off experiments. The simulated global mean LFRs by STD and Volca-off experiments are the  
 477 same until April 1991. They then begin to show differences from May 1991 (The time series of global mean LFRs is not  
 478 shown.). This result is reasonable because the Pinatubo volcanic perturbations are removed from SAC during June 1991 –  
 479 May 1996 in the Volca-off experiments by equation (11), and because the SAC of May 1991 used in CHASER is  
 480 interpolated between the SAC of April 1991 and June 1991.



481  
 482 **Figure 10: Time series of LFR anomalies during 1990–1999 or during 1991–1992. Panels (a) and (b) show the time series of LFR**  
 483 **anomalies and their smoothed curves by 1-D Gaussian (Denosing) filter for 1990–1999. Panels (c) and (d) present the time series of**

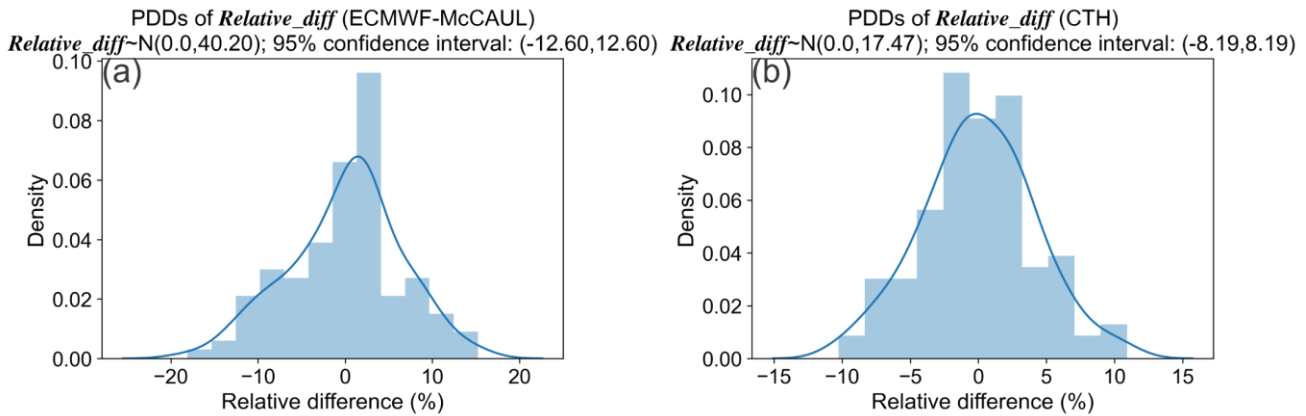
484 **LFR anomalies during 1991–1992.** Values shown over the red lines in panels (c) and (d) are *Relative\_diff* calculated using  
485 **equation 12.**

486

487 Figures 10c–10d portray the time series of LFR anomalies and *Relative\_diff* (values over the red lines) during 1991–  
488 1992. *Relative\_diff* are relative differences of the global mean LFR anomalies between STD and Volca-off experiments  
489 calculated using the following equation.

$$490 \text{ *Relative_diff* = 100\%} \times \frac{\text{LFR}_{STD} - \text{LFR}_{Volca-off}}{\text{LFR}_{Volca-off}} \quad (12)$$

491 In the equation,  $\text{LFR}_{STD}$  represents global mean LFR anomalies simulated by STD-F1/F2 experiments.  $\text{LFR}_{Volca-off}$   
492 denotes global mean LFR anomalies simulated by Volca-off-F1/F2 experiments.  $\text{LFR}_{Volca-off}$  symbolizes global mean  
493 LFRs simulated by Volca-off-F1/F2 experiments.

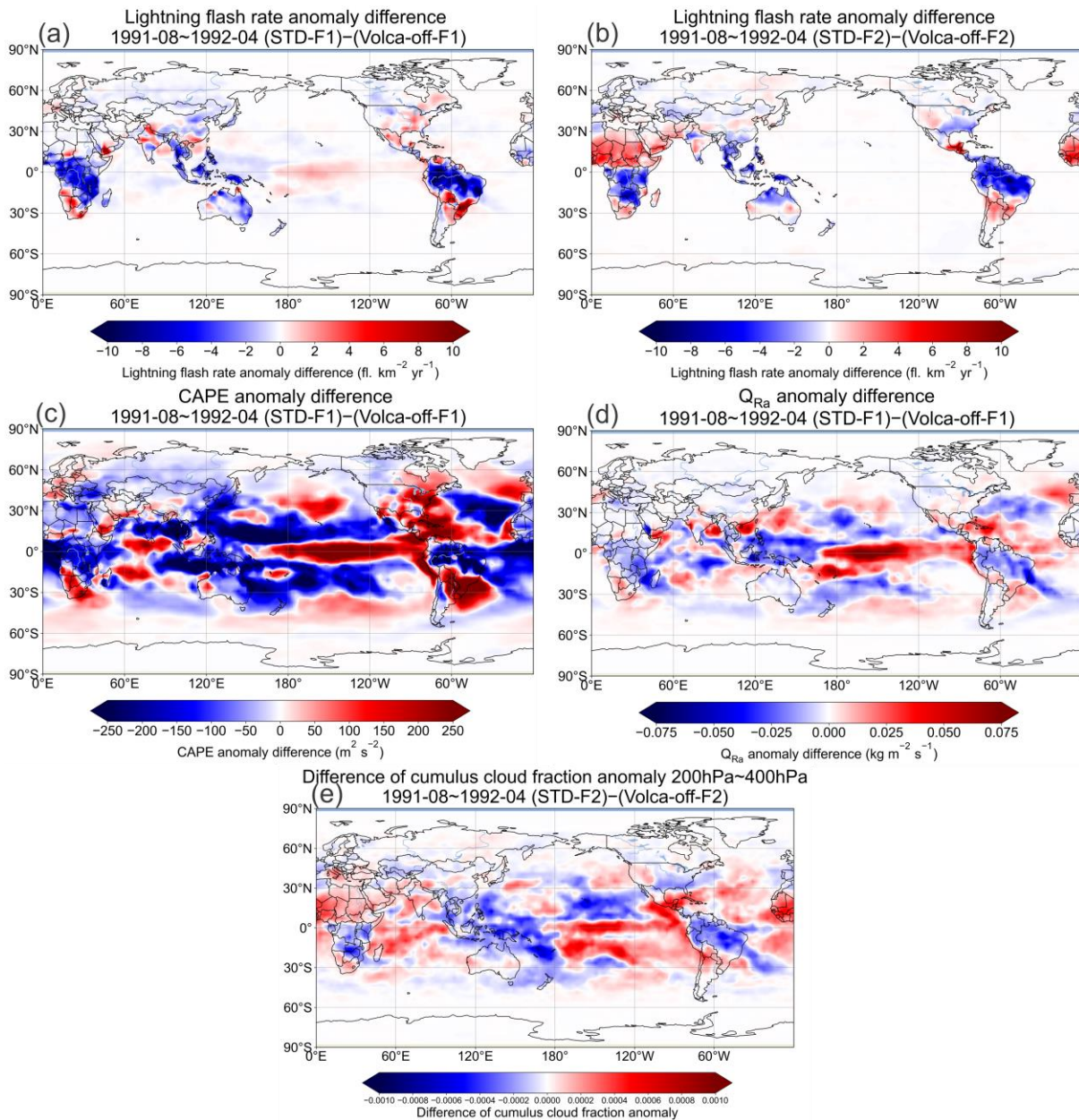


494

495 **Figure 11: Probability Density Distributions (PDDs) of *Relative\_diff* obtained from monthly time-series data of *Relative\_diff***  
496 **during 1990–1999. The 95% confidence interval of *Relative\_diff* is also shown in the titles of this figure.**

497

498 The monthly time-series data of *Relative\_diff* for 1990–1999 for both lightning schemes are calculated. The Probability  
499 Density Distributions (PDDs) of *Relative\_diff* are displayed in Fig. 11. The *Relative\_diff* presented in Fig. 11 are all  
500 normally distributed as determined by the Kolmogorov–Smirnov test. The 95% confidence interval of *Relative\_diff* is  
501 calculated and shown in the titles of Fig. 11. As displayed in Figs. 10c–10d, the underlined values (*Relative\_diff*)  
502 exceeded the 95% confidence interval, indicating significant differences in the calculated global mean LFR anomalies by  
503 STD and Volca-off experiments. In other words, global lightning activities were suppressed significantly by the Pinatubo  
504 eruption during the first year after the eruption.



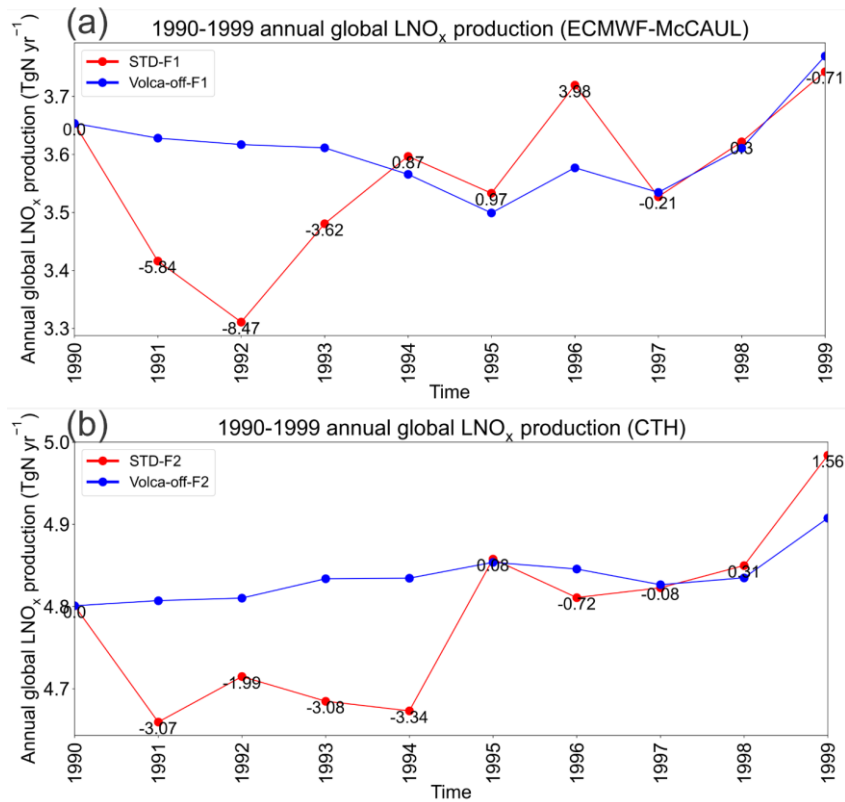
505

506 **Figure 12: 1991-08 – 1992-04 averaged LFR anomaly differences (a–b), CAPE anomaly differences (c),  $Q_{Ra}$  anomaly differences**  
 507 **(d), and differences of 200 hPa – 400 hPa averaged cumulus cloud fraction anomaly between STD-F2 and Volca-off-F2**  
 508 **experiments (e) on the global map.**

509

510 Figures 12a–12b show 1991-08 – 1992-04 averaged LFR anomaly differences between STD and Volca-off experiments on  
 511 the global map. We found from Figs. 12a–12b that lightning activities are suppressed significantly within the three hotspots  
 512 of lightning activities (Central Africa, Maritime Continent, and South America) during 1991-08 – 1992-04, when the global

513 mean LFRs are found to be suppressed. To elucidate the potential reasons for the suppressed global lightning activities  
 514 during the first year after the Pinatubo eruption, we first investigated the 1991-08 – 1992-04 averaged differences in CAPE  
 515 and  $Q_{Ra}$  anomaly between STD-F1 and Volca-off-F1 (Figs. 12c–12d) because lightning densities are computed with CAPE  
 516 and  $Q_{Ra}$  by the ECMWF-McCAUL scheme. Results showed that the Pinatubo eruption can engender apparent reductions of  
 517 CAPE and  $Q_{Ra}$  within tropical and subtropical terrestrial regions (typically three hotspots of lightning activities) where  
 518 lightning occurrence is frequent. These reductions constitute the main reason for the suppressed global lightning activities  
 519 during the first year after the Pinatubo eruption simulated by the ECMWF-McCAUL scheme. We also examined the 1991-  
 520 08 – 1992-04 averaged differences of 200 hPa – 400 hPa averaged cumulus cloud fraction anomaly between STD-F2 and  
 521 Volca-off-F2 on the global map (Fig. 12e). The cumulus cloud fractions of each model layer are used to weight the  
 522 calculated lightning densities from that layer by the CTH scheme, as explained in Sect. 2.2. As depicted in Fig. 12e and Fig.  
 523 S6, the Pinatubo eruption led to marked reductions in the middle to upper tropospheric cumulus cloud fractions during 1991-  
 524 08 – 1992-04 over three hotspots of lightning activities (Central Africa, Maritime Continent, and South America). As  
 525 displayed in Fig. 6f, the cumulus that reached the middle to upper troposphere is related closely to lightning formation.  
 526 Consequently, the simulated global lightning activities by the CTH scheme were also suppressed considerably during the  
 527 first year after the Pinatubo eruption.



528

529 **Figure 13: 1990–1999 annual global LNO<sub>x</sub> emissions calculated from the STD and Volca-off experiments’ outputs simulated using**  
530 **the ECMWF-McCAUL scheme (a) and the CTH scheme (b). Values over the red lines represent the relative differences (%)**  
531 **between the red lines and blue lines, calculated with respect to the blue lines.**

532

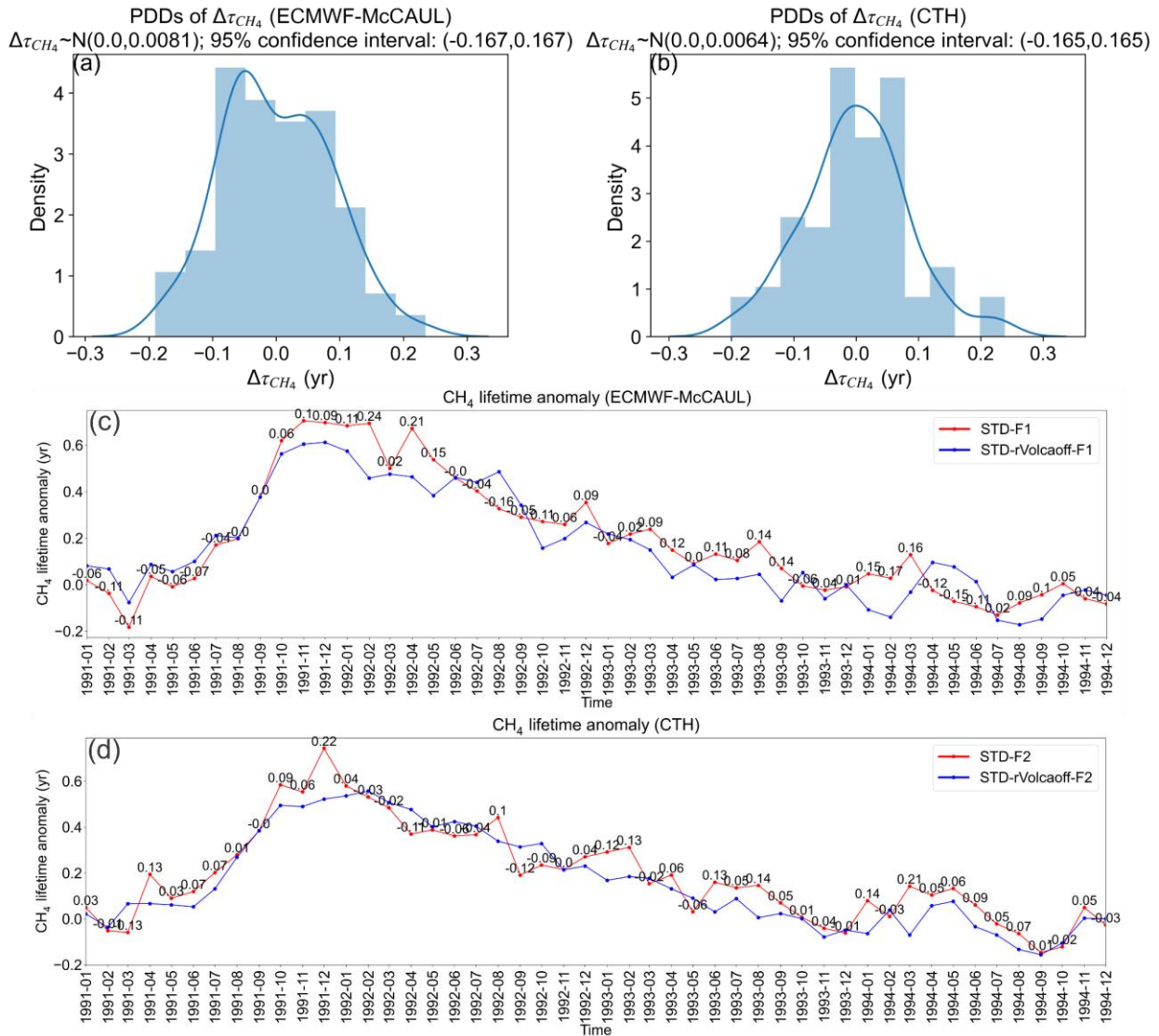
533 Aside from the global lightning activity suppression described earlier, the production of LNO<sub>x</sub> might also decrease after the  
534 Pinatubo eruption. To explore this conjecture, we compared the LNO<sub>x</sub> emissions in STD and Volca-off experiments (Fig. 13).  
535 In the case of the ECMWF-McCAUL scheme, the reduction of LNO<sub>x</sub> emissions caused by the Pinatubo eruption started in  
536 1991 (5.84%) and continued until 1993, with the highest percentage reduction occurring in 1992 (8.47%) (Fig. 13a).  
537 However, the CTH scheme showed a slightly different scenario of LNO<sub>x</sub> emissions reduction after the Pinatubo eruption.  
538 The LNO<sub>x</sub> emissions are almost evenly reduced during 1991–1994 in the case of the CTH scheme (Fig. 13b). In conclusion,  
539 our study indicates that the Pinatubo eruption can engender reductions in global LNO<sub>x</sub> emissions, which last 2–3 years.  
540 However, there exists some uncertainty in evaluating the magnitude of the reductions: from 1.99% to 8.47% for the annual  
541 percentage reduction found from our study.

542

543 The simulated reduced global LNO<sub>x</sub> emissions caused by the Pinatubo eruption might influence atmospheric chemistry  
544 significantly. Most importantly, the reduced global LNO<sub>x</sub> emissions might reduce OH radical production and extend the  
545 global mean tropospheric lifetime of methane against tropospheric OH radical, abbreviated hereinafter as the methane  
546 lifetime. We investigated this point further by comparing the methane lifetime anomaly simulated by STD and STD-  
547 rVolcaoff experiments. As introduced in Sect. 2.5, the settings of STD-rVolcaoff experiments are the same as those use for  
548 STD experiments, except that they use the daily LNO<sub>x</sub> emission rates calculated from the Volca-off experiments. We  
549 calculated the monthly CH<sub>4</sub> lifetime anomalies during 1990–1999 and  $\Delta\tau_{CH_4}$  (the difference of CH<sub>4</sub> lifetime anomaly  
550 between STD and STD-rVolcaoff experiments), which are shown in Figs. 14c–14d. Figures 14a–14b display the PDDs of  
551  $\Delta\tau_{CH_4}$  monthly time series during 1990–1999. The  $\Delta\tau_{CH_4}$  shown in Figs. 14a–14b are all normally distributed, as determined  
552 using the Kolmogorov–Smirnov test. The 95% confidence interval of  $\Delta\tau_{CH_4}$  is calculated and shown in the titles of Figs.  
553 14a–14b. The annual global LNO<sub>x</sub> production averaged during 1990–1999 is 3.56 TgN yr<sup>-1</sup> for STD-F1 and 4.79 TgN yr<sup>-1</sup>  
554 for STD-F2. At this level of annual global LNO<sub>x</sub> production, we found that within the first two years after the Pinatubo  
555 eruption, the  $\Delta\tau_{CH_4}$  exceeded the 95% confidence interval simulated by both lighting schemes (1992-02 and 1992-04 in the  
556 case of the ECMWF-McCAUL scheme; 1991-12 in the case of the CTH scheme). However, the widely cited range of annual  
557 global LNO<sub>x</sub> production is 2–8 TgN yr<sup>-1</sup> (Schumann and Huntrieser, 2007). Presuming that  $\Delta\tau_{CH_4}$  responds linearly to the  
558 LNO<sub>x</sub> emission level, and that the annual global LNO<sub>x</sub> production is 8 TgN yr<sup>-1</sup>, then the extension of the CH<sub>4</sub> lifetime  
559 because of the reduced LNO<sub>x</sub> emissions can reach around 0.54 years for the ECMWF-McCAUL scheme. As a comparison,  
560 ultraviolet shielding effects caused by stratospheric aerosols after the Pinatubo eruption led to the maximum increase of the  
561 methane lifetime by about 0.6 years (Figs. 14c–14d).

562





563

564 **Figure 14:** Panels (a) and (b) show the Probability Density Distributions (PDDs) of  $\Delta\tau_{CH_4}$  obtained from the monthly time series  
 565 data of  $\Delta\tau_{CH_4}$  during 1990–1999.  $\Delta\tau_{CH_4}$  represents the difference in CH<sub>4</sub> lifetime anomaly between STD and STD-rVolcaoff  
 566 experiments. The 95% confidence interval of  $\Delta\tau_{CH_4}$  is also presented in the titles of panels (a)–(b). Panels (c) and (d) show monthly  
 567 time series of CH<sub>4</sub> lifetime anomalies simulated by STD-F1/F2 and STD-rVolcaoff-F1/F2 experiments. Values over the red lines  
 568 represent  $\Delta\tau_{CH_4}$ .

### 569 3.4 Model intercomparisons of LFR trends with CMIP6 model outputs

570 The historical lightning trends demonstrated in our study are undoubtedly worth comparing with the results of other  
 571 chemistry–climate models or Earth system models. As introduced in Sect. 2.4, for comparison of the simulated LFR trends

572 and variations in our study with those of other CMIP6 models' outputs, we used all available LFR data from the CMIP6  
573 CMIP Historical experiments from CESM2-WACCM (3 ensembles) (Danabasoglu, 2019), GISS-E2-1-G (9 ensembles)  
574 (Kelley et al., 2020), and UKESM1-0-LL (18 ensembles) (Tang et al., 2019). Table S1 presents a complete list of the  
575 ensemble members we used. It is noteworthy that the LFR data obtained from the three CMIP6 models described earlier are  
576 calculated using the CTH scheme. The results of model intercomparisons of LFR trends and variations are displayed in Fig.  
577 15. As illustrated in Figs. 15a–15b, both the ECMWF-McCAUL and the CTH schemes (STD-F1/F2) simulated almost flat  
578 statistically non-significant global lightning trends, but the ensemble mean obtained from another three CMIP6 models  
579 exhibit significant increasing global lightning trends (trends from  $0.11\% \text{ yr}^{-1}$  to  $0.25\% \text{ yr}^{-1}$ ). Many reasons underlie the  
580 differences in global lightning trends simulated by CHASER in our study and by the three CMIP6 models, including the use  
581 of different methods to determine SSTs/sea ice fields. Instead of using a coupled Atmosphere–Ocean general circulation  
582 model to calculate SSTs/sea ice fields dynamically in the three CMIP6 models, CHASER uses the prescribed HadISST data  
583 (Rayner et al., 2003), which are based on plenty of observational data. Changes in the global mean sea surface temperature  
584 anomaly during 1960–2014 ( $\Delta\text{SST}$ ) obtained from STD-F1/F2 and CMIP6 model outputs are presented in Table 2. We also  
585 used the observation-based Extended Reconstructed SST (ERSST) dataset (Huang et al., 2017) constructed by NOAA to  
586 evaluate the  $\Delta\text{SST}$  obtained from different models. The  $\Delta\text{SST}$  calculated from ERSST during 1960–2014 is  $0.549^\circ\text{C}$ , which  
587 most closely approximates the  $\Delta\text{SST}$  obtained from STD-F1/F2. Considered from the perspective of SSTs/sea ice fields  
588 alone, the results (global lightning trends) of our study are expected to be closer to the actual situation.

589

590 Actually, the three CMIP6 models simulated stronger global warming during 1960–2014 than CHASER in our study, as  
591 displayed in Fig. S7. The CTH scheme is reported to respond positively to simulated global warming (Price and Rind, 1994;  
592 Zeng et al., 2008; Hui and Hong, 2013; Banerjee et al., 2014; Krause et al., 2014; Clark et al., 2017). The simulated stronger  
593 global warming by the three CMIP6 models is regarded as responsible for differences in simulated global lightning trends  
594 between our study and the three CMIP6 models (Figs. 15a–15b). We further investigated the sensitivities of the global mean  
595 LFR anomaly change to the global mean surface temperature anomaly increase ( $\% \text{ }^\circ\text{C}^{-1}$ ) obtained from CHASER and the  
596 three CMIP6 models. The sensitivities in percentage per degree Celsius are presented in Table 2. Overall, even when using  
597 the same CTH scheme, the sensitivities ( $\Delta\text{LFR}/\Delta\text{TS}$ ) simulated by the three CMIP6 models are higher than that simulated by  
598 CHASER in our study. This different sensitivity might be partially attributable to the nonlinear relation between lightning  
599 response and climate change (Pinto, 2013; Krause et al., 2014). Compared to the CTH scheme, the ECMWF-McCAUL  
600 scheme simulated a statistically non-significant negative sensitivity ( $\Delta\text{LFR}/\Delta\text{TS}$ ), which is attributable to the stronger  
601 suppression of positive global lightning trends caused by increases in AeroPEs simulated using the ECMWF-McCAUL  
602 scheme.

603

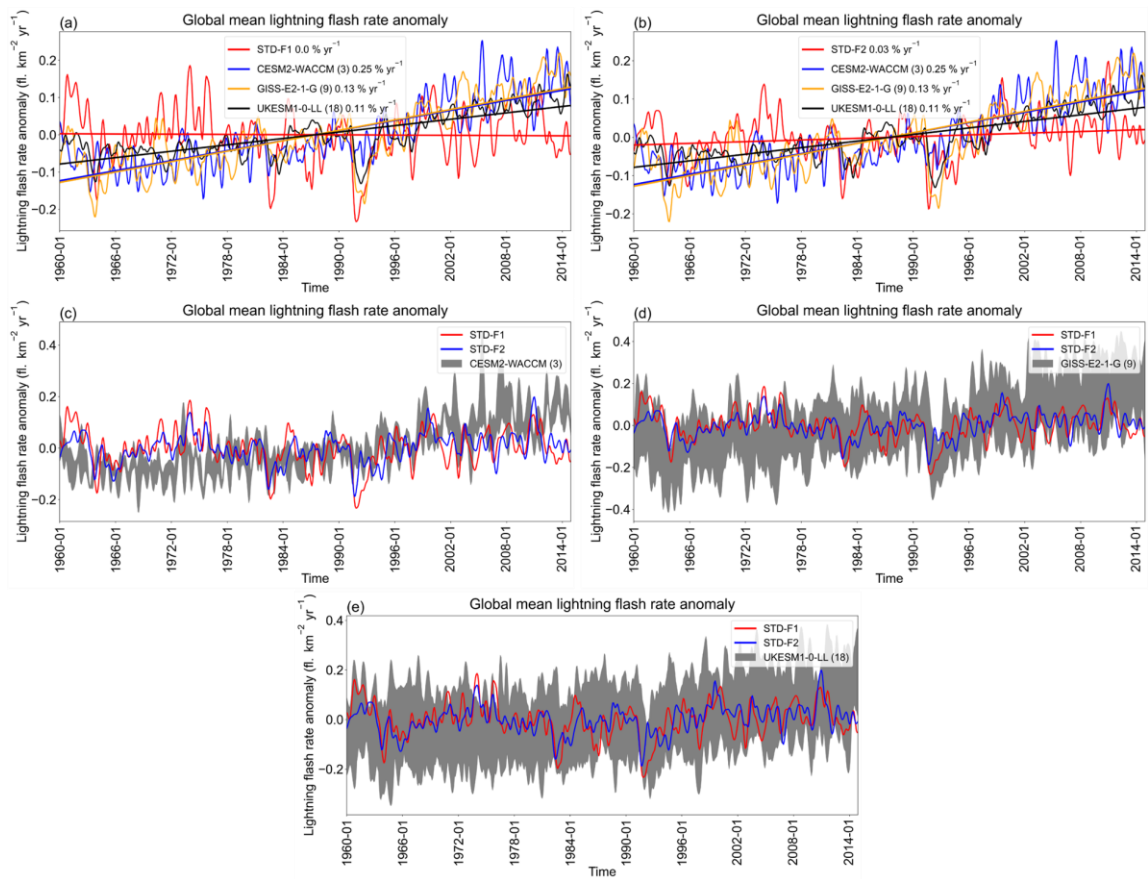
604 **Table 2: Changes in global mean surface temperature anomaly ( $\Delta\text{TS}$ ), global mean sea surface temperature anomaly ( $\Delta\text{SST}$ ),**  
605 **global mean lightning flash rate anomaly ( $\Delta\text{LFR}$ ), and the rate of change of LFR anomaly corresponding to each degree-Celsius**

606 increase in global mean surface temperature anomaly ( $\Delta\text{LFR}/\Delta\text{TS}$ ) obtained from STD-F1/F2 and CMIP6 model outputs. The  
 607 change of  $\Delta\text{SST}$  obtained from the ERSST dataset is also shown in this Table. Changes were obtained by calculating the difference  
 608 between the rightmost and leftmost points of the approximating curve for the 1960–2014 time-series data.

| Model/experiment/dataset | $\Delta\text{TS}$ ( $^{\circ}\text{C}$ ) | $\Delta\text{SST}$ ( $^{\circ}\text{C}$ ) | $\Delta\text{LFR}$ (%) | $\Delta\text{LFR}/\Delta\text{TS}$ ( $\% \text{ } ^{\circ}\text{C}^{-1}$ ) |
|--------------------------|--|---|------------------------|--|
| STD-F1                   | 0.593                                    | 0.428                                     | -0.272                 | -0.46  |
| STD-F2                   | 0.563                                    | 0.432                                     | 1.497                  | 2.66   |
| CESM2-WACCM              | 1.245                                    | 1.077                                     | 13.758                 | 11.05  |
| GISS-E2-1-G              | 0.810                                    | 0.677                                     | 7.248                  | 8.95   |
| UKESM1-0-LL              | 1.141                                    | 0.999                                     | 5.942                  | 5.21   |
| ERSST                    | —  | 0.549                                     | —                      | —  |

609

610 Figures 15d–15e affirm that the global lightning variation simulated by our study is basically within the full ensemble range  
 611 of GISS-E2-1-G and UKESM1-0-LL. After the Pinatubo eruption, as described in Sect. 3.3 of this report, the GISS-E2-1-G  
 612 and UKESM1-0-LL models also manifest significant suppression of global lightning activities, but the CESM2-WACCM  
 613 model shows no such phenomenon. The commonalities and differences in global lightning trends and variations found in the  
 614 model intercomparisons imply that great uncertainties existed in past (1960–2014) global lightning trend simulations. Such  
 615 uncertainties deserve to be investigated further.



616

617 **Figure 15: Comparisons of simulated global mean LFR anomalies found in our study (CHASER) and found using other CMIP6**  
 618 **models. All the figures are created based on the monthly time-series data of global mean LFR anomalies with a 1-D Gaussian**  
 619 **(Denoising) filter applied. For CMIP6 models, the ensemble mean is shown as the solid line, and the full ensemble range is shown**  
 620 **as grey shading (c–e). Fitting curves and the trends of fitting curves ( $\% \text{ yr}^{-1}$ ) are also given in (a–b).**

#### 621 4 Discussion and Conclusions

622 We used two lightning schemes (the CTH and ECMWF-McCAUL schemes) to study historical (1960–2014) lightning–  
 623  $\text{LNO}_x$  trends and variations and their influencing factors (global warming, increases in AeroPEs, and Pinatubo eruption)  
 624 within the CHASER (MIROC) chemistry–climate model. The CTH scheme, which is the most widely used lightning scheme,  
 625 nevertheless lacks a direct physical link with the charging mechanism. The ECMWF-McCAUL scheme is a newly  
 626 developed process-based/ice-based lightning scheme with a direct physical link to the charging mechanism.

627

628 With only the aerosol radiative effects considered in the lightning–aerosols interaction, both lightning schemes simulated  
 629 almost flat trends of global mean LFR during 1960–2014. Reportedly, because the aerosol microphysical effects can enhance

630 lightning activities (Yuan et al., 2011; Wang et al., 2018; Liu et al., 2020), our study might underestimate the increasing  
631 trend of global mean LFR (our study only considered the aerosol radiative effects in aerosol–lightning interactions). Further  
632 research is anticipated, with consideration of the effects of aerosol microphysical effects on long-term lightning trends.  
633 Moreover, both lightning schemes manifest that past global warming enhances the historical trend of global mean lightning  
634 density toward the positive direction (around  $0.03\% \text{ yr}^{-1}$  or  $3\% \text{ K}^{-1}$ ). However, past increases in AeroPEs exert the opposite  
635 effect to the lightning trend ( $-0.07\% \text{ yr}^{-1}$  –  $-0.04\% \text{ yr}^{-1}$ ). The effects of the increased AeroPEs on the lightning trend only  
636 over land regions expand to  $-0.10\% \text{ yr}^{-1}$  –  $-0.05\% \text{ yr}^{-1}$ , which implies that the effects are more significant over land regions.  
637 We obtained similar results for the historical global  $\text{LNO}_x$  emissions trend, which indicates that historical global warming  
638 and increases in AeroPEs can affect atmospheric chemistry and engender feedback by influencing  $\text{LNO}_x$  emissions.  
639 Although the CTH and ECMWF-McCAUL schemes use different parameters to simulate lightning, both lightning schemes  
640 indicate that the enhanced global convective activity under global warming is the main reason for the increase in lightning–  
641  $\text{LNO}_x$  emissions. In contrast, the increases in AeroPEs have decreased lightning– $\text{LNO}_x$  emissions by weakening the  
642 convective activity in the lightning hotspots. By analyzing the simulation results on the global map, we also found that the  
643 effects of historical global warming and increases in AeroPEs on lightning trends are heterogeneous across different regions.  
644 Our results indicate that historical global warming enhances lightning activities within the Arctic region and Japan but  
645 suppresses lightning activities around New Zealand and some parts of the Southern Ocean. Both lightning schemes  
646 demonstrated that the historical increases in AeroPEs suppress lightning activities in some parts of the Southern Ocean and  
647 South America. The ECMWF-McCAUL scheme also suggests that historical increases in AeroPEs suppress lightning  
648 activities in some parts of India and China when only the aerosol radiative effects are considered. This finding is plausible  
649 because both countries experienced dramatic increases in AeroPEs during 1960–2014 because of rapid economic growth.

650  
651 Furthermore, this report is the first describing significant suppression of global lightning activity during the first year after  
652 the Pinatubo eruption, which is indicated in both lightning schemes (global lightning activities decreased by up to 18.10%  
653 simulated by the ECMWF-McCAUL scheme). This finding is mainly attributable to the Pinatubo eruption weakening of the  
654 convective activities within the hotspots of lightning, which in turn decreased  $Q_{Ra}$  and middle-level to high-level cumulus  
655 cloud fractions in these regions. The simulation results also indicate that the Pinatubo eruption can engender reductions in  
656 global  $\text{LNO}_x$  emissions, which last 2–3 years. However, some uncertainty exists in evaluating magnitude of these reductions  
657 (from 1.99% to 8.47% for the annual percentage reduction in our study). The case study of the Pinatubo eruption in our  
658 research indicates that other large-scale volcanic eruptions can also engender significant reduction of global lightning  
659 activities and global-scale  $\text{LNO}_x$  emissions.

660  
661 Lastly, we compared the global lightning trends demonstrated in our study with the outputs of three CMIP6 models:  
662 CESM2-WACCM, GISS-E2-1-G, and UKESM1-0-LL. We used all available LFR data from the CMIP6 CMIP historical  
663 experiments from the three models described above. The three CMIP6 models suggest significant increasing trends in

664 historical global lightning activities, which differs from the findings of our study. Unlike the three CMIP6 models which use  
665 a coupled Atmosphere–Ocean general circulation model to calculate SSTs/sea ice fields dynamically, our study (CHASER)  
666 uses the prescribed HadISST SSTs/sea ice data, which more closely reflect the actual situation. Therefore, we believe that  
667 the results (the historical global lightning trends) obtained from our study (CHASER) more closely approximate the actual  
668 situation. However, model intercomparisons of global lightning trends still indicate that considerable uncertainties exist in  
669 historical (1960–2014) global lightning trend simulations, and that such uncertainties deserve further investigation.

#### 670 **Code availability**

671 The source code for CHASER to reproduce results obtained from this work is obtainable from the repository at  
672 <https://doi.org/10.5281/zenodo.5835796> (He et al., 2022a).

#### 673 **Data availability**

674 The LIS/OTD data used for this study are available from <https://ghrc.nsstc.nasa.gov/hydro/?q=LRTS> (last access: 11 January  
675 2022). The CMIP6 model outputs (LFR and surface temperature) used for this study are available from  
676 <https://aims2.llnl.gov/search> (last access: 1 February 2023). The Extended Reconstructed SST data used for this study are  
677 available from <https://www.ncei.noaa.gov/products/extended-reconstructed-sst> (last access: 27 March 27 2023).

#### 678 **Author contributions**

679 YFH conducted all simulations, interpreted the results, and wrote the manuscript. KS developed the CHASER (MIROC)  
680 model code, conceived the presented idea, and supervised the findings of this work and the manuscript preparation.

#### 681 **Competing interests**

682 The authors declare that they have no conflict of interest.

#### 683 **Acknowledgments**

684 This research was supported by the Global Environment Research Fund (S–12 and S–20) of the Ministry of the Environment  
685 (MOE), Japan, and JSPS KAKENHI Grant Numbers: JP20H04320, JP19H05669, and JP19H04235. This work was  
686 supported by the Japan Science and Technology Agency (JST) Support for Pioneering Research Initiated by the Next  
687 Generation (SPRAINING), Grant Number JPMJSP2125. The author would like to take this opportunity to thank the  
688 “Interdisciplinary Frontier Next-Generation Researcher Program of the Tokai Higher Education and Research System.” The

689 simulations were completed using the supercomputer (NEC SX-Aurora TSUBASA) at NIES (Japan). We thank NASA  
690 scientists and staff for providing LIS/OTD lightning observation data. We acknowledge the World Climate Research  
691 Programme, which coordinated and promoted CMIP6 through its Working Group on Coupled Modelling. We extend our  
692 sincere gratitude to the climate modelling groups for producing and providing their model outputs, to the Earth System Grid  
693 Federation (ESGF) for archiving the data and providing free downloads, and to the multiple funding agencies that have  
694 supported the CMIP6 as well as the Earth System Grid Federation. We also thank Ms. Do Thi Nhu Ngoc for her assistance in  
695 downloading the CMIP6 model outputs.

## 696 **References**

- 697 Allen, D. J., Pickering, K. E., Bucsela, E., Krotkov, N., and Holzworth, R.: Lightning NO<sub>x</sub> Production in the Tropics as  
698 Determined Using OMI NO<sub>2</sub> Retrievals and WWLLN Stroke Data, *Journal of Geophysical Research: Atmospheres*,  
699 124, 13498–13518, <https://doi.org/10.1029/2018JD029824>, 2019.
- 700 Altartz, O., Kucienska, B., Kostinski, A., Raga, G. B., and Koren, I.: Global association of aerosol with flash density of  
701 intense lightning, *Environ. Res. Lett.*, 12, 114037, <https://doi.org/10.1088/1748-9326/aa922b>, 2017.
- 702 Arfeuille, F., Luo, B. P., Heckendorn, P., Weisenstein, D., Sheng, J. X., Rozanov, E., Schraner, M., Brönnimann, S.,  
703 Thomason, L. W., and Peter, T.: Modeling the stratospheric warming following the Mt. Pinatubo eruption:  
704 uncertainties in aerosol extinctions, *Atmospheric Chemistry and Physics*, 13, 11221–11234,  
705 <https://doi.org/10.5194/acp-13-11221-2013>, 2013.
- 706 Banerjee, A., Archibald, A. T., Maycock, A. C., Telford, P., Abraham, N. L., Yang, X., Braesicke, P., and Pyle, J. A.:  
707 Lightning NO<sub>x</sub>, a key chemistry–climate interaction: Impacts of future climate change and consequences for  
708 tropospheric oxidising capacity, *Atmospheric Chemistry and Physics*, 14, 9871–9881, [https://doi.org/10.5194/acp-14-](https://doi.org/10.5194/acp-14-9871-2014)  
709 9871-2014, 2014.
- 710 Boccippio, D. J., Koshak, W. J., and Blakeslee, R. J.: Performance Assessment of the Optical Transient Detector and  
711 Lightning Imaging Sensor. Part I: Predicted Diurnal Variability, *Journal of Atmospheric and Oceanic Technology*, 19,  
712 1318–1332, [https://doi.org/10.1175/1520-0426\(2002\)019<1318:PAOTOT>2.0.CO;2](https://doi.org/10.1175/1520-0426(2002)019<1318:PAOTOT>2.0.CO;2), 2002.
- 713 Boucher, O.: *Atmospheric Aerosols*, Springer Netherlands, Dordrecht, <https://doi.org/10.1007/978-94-017-9649-1>, 2015.
- 714 Bucsela, E. J., Pickering, K. E., Allen, D. J., Holzworth, R. H., and Krotkov, N. A.: Midlatitude Lightning NO<sub>x</sub> Production  
715 Efficiency Inferred From OMI and WWLLN Data, *Journal of Geophysical Research: Atmospheres*, 124, 13475–  
716 13497, <https://doi.org/10.1029/2019JD030561>, 2019.
- 717 Cecil, D. J., Buechler, D. E., and Blakeslee, R. J.: Gridded lightning climatology from TRMM-LIS and OTD: Dataset  
718 description, *Atmospheric Research*, 135–136, 404–414, <https://doi.org/10.1016/j.atmosres.2012.06.028>, 2014.
- 719 Cerveny, R. S., Bessemoulin, P., Burt, C. C., Cooper, M. A., Cunjie, Z., Dewan, A., Finch, J., Holle, R. L., Kalkstein, L.,  
720 Kruger, A., Lee, T., Martínez, R., Mohapatra, M., Pattanaik, D. R., Peterson, T. C., Sheridan, S., Trewin, B., Tait, A.,

721 and Wahab, M. M. A.: WMO Assessment of Weather and Climate Mortality Extremes: Lightning, Tropical Cyclones,  
722 Tornadoes, and Hail, *Weather, Climate, and Society*, 9, 487–497, <https://doi.org/10.1175/WCAS-D-16-0120.1>, 2017.

723 Clark, S. K., Ward, D. S., and Mahowald, N. M.: Parameterization-based uncertainty in future lightning flash density,  
724 *Geophysical Research Letters*, 44, 2893–2901, <https://doi.org/10.1002/2017GL073017>, 2017.

725 NOAA National Centers for Environmental Information (NCEI), *Climate at a Glance: Global Time Series*, published June  
726 2023, retrieved on January 10, 2023 from [https://www.ncei.noaa.gov/access/monitoring/climate-at-a-](https://www.ncei.noaa.gov/access/monitoring/climate-at-a-glance/global/time-series/globe/land_ocean/3/8/1880-2020)  
727 [glance/global/time-series/globe/land\\_ocean/3/8/1880-2020](https://www.ncei.noaa.gov/access/monitoring/climate-at-a-glance/global/time-series/globe/land_ocean/3/8/1880-2020).

728 Cooper, M. A. and Holle, R. L.: Current Global Estimates of Lightning Fatalities and Injuries, in: *Reducing Lightning*  
729 *Injuries Worldwide*, edited by Cooper, M. A. and Holle, R. L., Springer International Publishing, Cham, 65–73,  
730 [https://doi.org/10.1007/978-3-319-77563-0\\_6](https://doi.org/10.1007/978-3-319-77563-0_6), 2019.

731 Cooray, V., Rahman, M., and Rakov, V.: On the NO<sub>x</sub> production by laboratory electrical discharges and lightning, *Journal of*  
732 *Atmospheric and Solar–Terrestrial Physics*, 71, 1877–1889, <https://doi.org/10.1016/j.jastp.2009.07.009>, 2009.

733 Danabasoglu, G.: NCAR CESM2-WACCM model output prepared for CMIP6 CMIP historical,  
734 <https://doi.org/10.22033/ESGF/CMIP6.10071>, 2019.

735 Danabasoglu, G., Lamarque, J.-F., Bacmeister, J., Bailey, D. A., DuVivier, A. K., Edwards, J., Emmons, L. K., Fasullo, J.,  
736 Garcia, R., Gettelman, A., Hannay, C., Holland, M. M., Large, W. G., Lauritzen, P. H., Lawrence, D. M., Lenaerts, J.  
737 T. M., Lindsay, K., Lipscomb, W. H., Mills, M. J., Neale, R., Oleson, K. W., Otto-Bliesner, B., Phillips, A. S., Sacks,  
738 W., Tilmes, S., van Kampenhout, L., Vertenstein, M., Bertini, A., Dennis, J., Deser, C., Fischer, C., Fox-Kemper, B.,  
739 Kay, J. E., Kinnison, D., Kushner, P. J., Larson, V. E., Long, M. C., Mickelson, S., Moore, J. K., Nienhouse, E.,  
740 Polvani, L., Rasch, P. J., and Strand, W. G.: The Community Earth System Model Version 2 (CESM2), *Journal of*  
741 *Advances in Modeling Earth Systems*, 12, e2019ms001916, <https://doi.org/10.1029/2019ms001916>, 2020.

742 Del Genio, A. D., Yao, M.-S., and Jonas, J.: Will moist convection be stronger in a warmer climate?, *Geophysical Research*  
743 *Letters*, 34, <https://doi.org/10.1029/2007GL030525>, 2007.

744 Finney, D. L., Doherty, R. M., Wild, O., and Abraham, N. L.: The impact of lightning on tropospheric ozone chemistry using  
745 a new global lightning parametrisation, *Atmospheric Chemistry and Physics*, 16, 7507–7522,  
746 <https://doi.org/10.5194/acp-16-7507-2016>, 2016b.

747 Finney, D. L., Doherty, R. M., Wild, O., Huntrieser, H., Pumphrey, H. C., and Blyth, A. M.: Using cloud ice flux to  
748 parametrise large-scale lightning, *Atmospheric Chemistry and Physics*, 14, 12665–12682, [https://doi.org/10.5194/acp-](https://doi.org/10.5194/acp-14-12665-2014)  
749 [14-12665-2014](https://doi.org/10.5194/acp-14-12665-2014), 2014.

750 Finney, D. L., Doherty, R. M., Wild, O., Stevenson, D. S., MacKenzie, I. A., and Blyth, A. M.: A projected decrease in  
751 lightning under climate change, *Nature Climate Change*, 8, 210–213, <https://doi.org/10.1038/s41558-018-0072-6>,  
752 2018.

753 Finney, D. L., Doherty, R. M., Wild, O., Young, P. J., and Butler, A.: Response of lightning NO<sub>x</sub> emissions and ozone  
754 production to climate change: Insights from the Atmospheric Chemistry and Climate Model Intercomparison Project,



755 Geophysical Research Letters, 43, 5492–5500, <https://doi.org/10.1002/2016GL068825>, 2016a.

756 Fujibe, F.: Long-term Change in Lightning Mortality and Its Relation to Annual Thunder Days in Japan, *Journal of Natural*  
757 *Disaster Science*, 38, 17–29, <https://doi.org/10.2328/jnds.38.17>, 2017.

758 Goodman, S. J., Buechler, D. E., and Wright, P. D.: Lightning/rainfall relationships during COHMEX, NTRS Author  
759 Affiliations: NASA Marshall Space Flight Center, Universities Space Research Association NTRS Document ID:  
760 19900057799 NTRS Research Center: Legacy CDMS (CDMS), 1990.

761 Goto, D., Nakajima, T., Dai, T., Takemura, T., Kajino, M., Matsui, H., Takami, A., Hatakeyama, S., Sugimoto, N., Shimizu,  
762 A., and Ohara, T.: An evaluation of simulated particulate sulfate over East Asia through global model intercomparison,  
763 *Journal of Geophysical Research: Atmospheres*, 120, 6247–6270, <https://doi.org/10.1002/2014JD021693>, 2015.

764 Guenther, A. B., Jiang, X., Heald, C. L., Sakulyanontvittaya, T., Duhl, T., Emmons, L. K., and Wang, X.: The Model of  
765 Emissions of Gases and Aerosols from Nature ver. 2.1 (MEGAN2.1): an extended and updated framework for  
766 modeling biogenic emissions, *Geosci. Model Dev.*, 5, 1471–1492, <https://doi.org/10.5194/gmd-5-1471-2012>, 2012.

767 Ha, P. T. M., Matsuda, R., Kanaya, Y., Taketani, F., and Sudo, K.: Effects of heterogeneous reactions on tropospheric  
768 chemistry: A global simulation with the chemistry–climate model CHASER V4.0, *Geoscientific Model Development*,  
769 14, 3813–3841, <https://doi.org/10.5194/gmd-14-3813-2021>, 2021.

770 He, Y., Hoque, M. S. H., and Sudo, K.: Introducing new lightning schemes into the CHASER (MIROC) chemistry climate  
771 model, [Code], Zenodo, <https://doi.org/10.5281/zenodo.5835796>, 2022a.

772 He, Y., Hoque, H. M. S., and Sudo, K.: Introducing new lightning schemes into the CHASER (MIROC) chemistry–climate  
773 model, *Geoscientific Model Development*, 15, 5627–5650, <https://doi.org/10.5194/GMD-15-5627-2022>, 2022b.

774 Hoesly, R. M., Smith, S. J., Feng, L., Klimont, Z., Janssens-Maenhout, G., Pitkanen, T., Seibert, J. J., Vu, L., Andres, R. J.,  
775 Bolt, R. M., Bond, T. C., Dawidowski, L., Kholod, N., Kurokawa, J., Li, M., Liu, L., Lu, Z., Moura, M. C. P.,  
776 O'Rourke, P. R., and Zhang, Q.: Historical (1750–2014) anthropogenic emissions of reactive gases and aerosols from  
777 the Community Emissions Data System (CEDS), *Geosci. Model Dev.*, 11, 369–408, [https://doi.org/10.5194/gmd-11-](https://doi.org/10.5194/gmd-11-369-2018)  
778 [369-2018](https://doi.org/10.5194/gmd-11-369-2018), 2018.

779 Huang, B., Thorne, P. W., Banzon, V. F., Boyer, T., Chepurin, G., Lawrimore, J. H., Menne, M. J., Smith, T. M., Vose, R. S.,  
780 and Zhang, H.-M.: Extended Reconstructed Sea Surface Temperature, Version 5 (ERSSTv5): Upgrades, Validations,  
781 and Intercomparisons, *Journal of Climate*, 30, 8179–8205, <https://doi.org/10.1175/JCLI-D-16-0836.1>, 2017.

782 Hui, J. and Hong, L.: Projected Changes in NO<sub>x</sub> Emissions from Lightning as a Result of 2000–2050 Climate Change,  
783 *Atmospheric and Oceanic Science Letters*, 6, 284–289, <https://doi.org/10.3878/j.issn.1674-2834.13.0042>, 2013.

784 Hussain, Md. and Mahmud, I.: pyMannKendall: a python package for non parametric Mann Kendall family of trend tests.,  
785 *Journal of Open Source Software*, 4, 1556, <https://doi.org/10.21105/joss.01556>, 2019.

786 Ito, A. and Inatomi, M.: Water-use efficiency of the terrestrial biosphere: A model analysis focusing on interactions between  
787 the global carbon and water cycles, *Journal of Hydrometeorology*, 13, 681–694, [https://doi.org/10.1175/JHM-D-10-](https://doi.org/10.1175/JHM-D-10-05034.1)  
788 [05034.1](https://doi.org/10.1175/JHM-D-10-05034.1), 2012.

789 Jensen, J. D., Thurman, J., and Vincent, A. L.: Lightning Injuries, in: StatPearls, StatPearls Publishing, Treasure Island (FL),  
790 2022.

791 Kaufman, Y. J., Tanré, D., Holben, B. N., Mattoo, S., Remer, L. A., Eck, T. F., Vaughan, J., and Chatenet, B.: Aerosol  
792 Radiative Impact on Spectral Solar Flux at the Surface, Derived from Principal–Plane Sky Measurements, *Journal of*  
793 *the Atmospheric Sciences*, 59, 635–646, [https://doi.org/10.1175/1520-0469\(2002\)059<0635:AROSS>2.0.CO;2](https://doi.org/10.1175/1520-0469(2002)059<0635:AROSS>2.0.CO;2), 2002.

794 Kelley, M., Schmidt, G. A., Nazarenko, L. S., Bauer, S. E., Ruedy, R., Russell, G. L., Ackerman, A. S., Aleinov, I., Bauer,  
795 M., Bleck, R., Canuto, V., Cesana, G., Cheng, Y., Clune, T. L., Cook, B. I., Cruz, C. A., Del Genio, A. D., Elsaesser,  
796 G. S., Faluvegi, G., Kiang, N. Y., Kim, D., Lacis, A. A., Leboissetier, A., LeGrande, A. N., Lo, K. K., Marshall, J.,  
797 Matthews, E. E., McDermid, S., Mezuman, K., Miller, R. L., Murray, L. T., Oinas, V., Orbe, C., García-Pando, C. P.,  
798 Perlwitz, J. P., Puma, M. J., Rind, D., Romanou, A., Shindell, D. T., Sun, S., Tausnev, N., Tsigaridis, K., Tselioudis,  
799 G., Weng, E., Wu, J., and Yao, M.-S.: GISS-E2.1: Configurations and Climatology, *Journal of Advances in Modeling*  
800 *Earth Systems*, 12, e2019 ms002025, <https://doi.org/10.1029/2019 ms002025>, 2020.

801 Koren, I., Kaufman, Y. J., Remer, L. A., and Martins, J. V.: Measurement of the Effect of Amazon Smoke on Inhibition of  
802 Cloud Formation, *Science*, 303, 1342–1345, <https://doi.org/10.1126/science.1089424>, 2004.

803 Koren, I., Martins, J. V., Remer, L. A., and Afargan, H.: Smoke Invigoration Versus Inhibition of Clouds over the Amazon,  
804 *Science*, 321, 946–949, <https://doi.org/10.1126/science.1159185>, 2008.

805 Krause, A., Kloster, S., Wilkenskjeld, S., and Paeth, H.: The sensitivity of global wildfires to simulated past, present, and  
806 future lightning frequency, *Journal of Geophysical Research: Biogeosciences*, 119, 312–322,  
807 <https://doi.org/10.1002/2013JG002502>, 2014.

808 Labrador, L. J., von Kuhlmann, R., and Lawrence, M. G.: The effects of lightning-produced NO<sub>x</sub> and its vertical distribution  
809 on atmospheric chemistry: sensitivity simulations with MATCH-MPIC, *Atmospheric Chemistry and Physics*, 5,  
810 1815–1834, <https://doi.org/10.5194/acp-5-1815-2005>, 2005.

811 Lal, D. M., Ghude, S. D., Mahakur, M., Waghmare, R. T., Tiwari, S., Srivastava, M. K., Meena, G. S., and Chate, D. M.:  
812 Relationship between aerosol and lightning over Indo-Gangetic Plain (IGP), India, *Clim Dyn*, 50, 3865–3884,  
813 <https://doi.org/10.1007/s00382-017-3851-2>, 2018.

814 Li, Z., Guo, J., Ding, A., Liao, H., Liu, J., Sun, Y., Wang, T., Xue, H., Zhang, H., and Zhu, B.: Aerosol and boundary-layer  
815 interactions and impact on air quality, *National Science Review*, 4, 810–833, <https://doi.org/10.1093/nsr/nwx117>,  
816 2017.

817 Liaskos, C. E., Allen, D. J., and Pickering, K. E.: Sensitivity of tropical tropospheric composition to lightning NO<sub>x</sub>  
818 production as determined by replay simulations with GEOS-5, *Journal of Geophysical Research*, 120, 8512–8534,  
819 <https://doi.org/10.1002/2014JD022987>, 2015.

820 Liu, Y., Guha, A., Said, R., Williams, E., Lapierre, J., Stock, M., and Heckman, S.: Aerosol Effects on Lightning  
821 Characteristics: A Comparison of Polluted and Clean Regimes, *Geophysical Research Letters*, 47, e2019GL086825,  
822 <https://doi.org/10.1029/2019GL086825>, 2020.

823 Lopez, P.: A lightning parameterization for the ECMWF integrated forecasting system, *Monthly Weather Review*, 144,  
824 3057–3075, <https://doi.org/10.1175/MWR-D-16-0026.1>, 2016.

825 Manabe, S. and Wetherald, R. T.: The Effects of Doubling the CO<sub>2</sub> Concentration on the climate of a General Circulation  
826 Model, *Journal of the Atmospheric Sciences*, 32, 3–15, [https://doi.org/10.1175/1520-0469\(1975\)032<0003:TEODTC>2.0.CO;2](https://doi.org/10.1175/1520-0469(1975)032<0003:TEODTC>2.0.CO;2), 1975.

828 van Marle, M. J. E., Kloster, S., Magi, B. I., Marlon, J. R., Daniiau, A.-L., Field, R. D., Arneeth, A., Forrest, M., Hantson, S.,  
829 Kehrwald, N. M., Knorr, W., Lasslop, G., Li, F., Mangeon, S., Yue, C., Kaiser, J. W., and van der Werf, G. R.:  
830 Historic global biomass burning emissions for CMIP6 (BB4CMIP) based on merging satellite observations with  
831 proxies and fire models (1750–2015), *Geosci. Model Dev.*, 10, 3329–3357, [https://doi.org/10.5194/gmd-10-3329-](https://doi.org/10.5194/gmd-10-3329-2017)  
832 2017, 2017.

833 McCaul, E. W., Goodman, S. J., LaCasse, K. M., and Cecil, D. J.: Forecasting lightning threat using cloud-resolving model  
834 simulations, *Weather and Forecasting*, 24, 709–729, <https://doi.org/10.1175/2008WAF2222152.1>, 2009.

835 Meinshausen, M., Vogel, E., Nauels, A., Lorbacher, K., Meinshausen, N., Etheridge, D. M., Fraser, P. J., Montzka, S. A.,  
836 Rayner, P. J., Trudinger, C. M., Krummel, P. B., Beyerle, U., Canadell, J. G., Daniel, J. S., Enting, I. G., Law, R. M.,  
837 Lunder, C. R., O’Doherty, S., Prinn, R. G., Reimann, S., Rubino, M., Velders, G. J. M., Vollmer, M. K., Wang, R. H.  
838 J., and Weiss, R.: Historical greenhouse gas concentrations for climate modelling (CMIP6), *Geoscientific Model*  
839 *Development*, 10, 2057–2116, <https://doi.org/10.5194/gmd-10-2057-2017>, 2017.

840 Miller, R. L., Schmidt, G. A., Nazarenko, L. S., Tausnev, N., Bauer, S. E., DelGenio, A. D., Kelley, M., Lo, K. K., Ruedy,  
841 R., Shindell, D. T., Aleinov, I., Bauer, M., Bleck, R., Canuto, V., Chen, Y., Cheng, Y., Clune, T. L., Faluvegi, G.,  
842 Hansen, J. E., Healy, R. J., Kiang, N. Y., Koch, D., Lacis, A. A., LeGrande, A. N., Lerner, J., Menon, S., Oinas, V.,  
843 Pérez García-Pando, C., Perlwitz, J. P., Puma, M. J., Rind, D., Romanou, A., Russell, G. L., Sato, M., Sun, S.,  
844 Tsigaridis, K., Unger, N., Voulgarakis, A., Yao, M.-S., and Zhang, J.: CMIP5 historical simulations (1850–2012) with  
845 GISS ModelE2, *Journal of Advances in Modeling Earth Systems*, 6, 441–478, <https://doi.org/10.1002/2013ms000266>,  
846 2014.

847 Murray, L. T.: Lightning NO<sub>x</sub> and Impacts on Air Quality, *Current Pollution Reports*, 2, 115–133,  
848 <https://doi.org/10.1007/s40726-016-0031-7>, 2016.

849 Ott, L. E., Pickering, K. E., Stenchikov, G. L., Allen, D. J., DeCaria, A. J., Ridley, B., Lin, R. F., Lang, S., and Tao, W. K.:  
850 Production of lightning NO<sub>x</sub> and its vertical distribution calculated from three-dimensional cloud-scale chemical  
851 transport model simulations, *Journal of Geophysical Research Atmospheres*, 115, 4301,  
852 <https://doi.org/10.1029/2009JD011880>, 2010.

853 Pinto, O.: Lightning and climate: A review, in: 2013 International Symposium on Lightning Protection (XII SIPDA), 2013  
854 International Symposium on Lightning Protection (XII SIPDA), journalAbbreviation: 2013 International Symposium  
855 on Lightning Protection (XII SIPDA), 402–404, <https://doi.org/10.1109/SIPDA.2013.6729250>, 2013.

856 Price, C. and Rind, D.: A simple lightning parameterization for calculating global lightning distributions, *Journal of*

857 Geophysical Research, 97, 9919–9933, <https://doi.org/10.1029/92JD00719>, 1992.

858 Price, C. and Rind, D.: What determines the cloud-to-ground lightning fraction in thunderstorms?, Geophysical Research  
859 Letters, 20, 463–466, <https://doi.org/10.1029/93GL00226>, 1993.

860 Price, C. and Rind, D.: Possible implications of global climate change on global lightning distributions and frequencies,  
861 Journal of Geophysical Research, 99, 823–833, <https://doi.org/10.1029/94jd00019>, 1994.

862 Rayner, N. A., Parker, D. E., Horton, E. B., Folland, C. K., Alexander, L. V., Rowell, D. P., Kent, E. C., and Kaplan, A.:  
863 Global analyses of sea surface temperature, sea ice, and night marine air temperature since the late nineteenth century,  
864 Journal of Geophysical Research: Atmospheres, 108, <https://doi.org/10.1029/2002jd002670>, 2003.

865 Ridley, B. A., Pickering, K. E., and Dye, J. E.: Comments on the parameterization of lightning-produced NO in global  
866 chemistry-transport models, Atmospheric Environment, 39, 6184–6187,  
867 <https://doi.org/10.1016/j.atmosenv.2005.06.054>, 2005.

868 Romps, D. M.: Evaluating the Future of Lightning in Cloud-Resolving Models, Geophysical Research Letters, 46, 14863–  
869 14871, <https://doi.org/10.1029/2019GL085748>, 2019.

870 Romps, D. M., Seeley, J. T., Vollaro, D., and Molinari, J.: Projected increase in lightning strikes in the united states due to  
871 global warming, Science, 346, 851–854, <https://doi.org/10.1126/science.1259100>, 2014.

872 Sato, M., Hansen, J. E., McCormick, M. P., and Pollack, J. B.: Stratospheric aerosol optical depths, 1850–1990, Journal of  
873 Geophysical Research: Atmospheres, 98, 22987–22994, <https://doi.org/10.1029/93JD02553>, 1993.

874 Saunders, C. P. R., Keith, W. D., and Mitzeva, R. P.: The effect of liquid water on thunderstorm charging, Journal of  
875 Geophysical Research: Atmospheres, 96, 11007–11017, <https://doi.org/10.1029/91JD00970>, 1991.

876 Schumann, U. and Huntrieser, H.: The global lightning-induced nitrogen oxides source, Atmospheric Chemistry and Physics,  
877 7, 3823–3907, <https://doi.org/10.5194/acp-7-3823-2007>, 2007.

878 Sekiguchi, M. and Nakajima, T.: A k-distribution-based radiation code and its computational optimization for an  
879 atmospheric general circulation model, Journal of Quantitative Spectroscopy and Radiative Transfer, 109, 2779–2793,  
880 <https://doi.org/10.1016/j.jqsrt.2008.07.013>, 2008.

881 Sellar, A. A., Jones, C. G., Mulcahy, J. P., Tang, Y., Yool, A., Wiltshire, A., O’Connor, F. M., Stringer, M., Hill, R.,  
882 Palmieri, J., Woodward, S., de Mora, L., Kuhlbrodt, T., Rumbold, S. T., Kelley, D. I., Ellis, R., Johnson, C. E.,  
883 Walton, J., Abraham, N. L., Andrews, M. B., Andrews, T., Archibald, A. T., Berthou, S., Burke, E., Blockley, E.,  
884 Carslaw, K., Dalvi, M., Edwards, J., Folberth, G. A., Gedney, N., Griffiths, P. T., Harper, A. B., Hendry, M. A.,  
885 Hewitt, A. J., Johnson, B., Jones, A., Jones, C. D., Keeble, J., Liddicoat, S., Morgenstern, O., Parker, R. J., Predoi, V.,  
886 Robertson, E., Siahann, A., Smith, R. S., Swaminathan, R., Woodhouse, M. T., Zeng, G., and Zerroukat, M.:  
887 UKESM1: Description and Evaluation of the U.K. Earth System Model, Journal of Advances in Modeling Earth  
888 Systems, 11, 4513–4558, <https://doi.org/10.1029/2019ms001739>, 2019.

889 Shi, Z., Wang, H., Tan, Y., Li, L., and Li, C.: Influence of aerosols on lightning activities in central eastern parts of China,  
890 Atmospheric Science Letters, 21, e957, <https://doi.org/10.1002/asl.957>, 2020.

891 Soden, B. J., Wetherald, R. T., Stenchikov, G. L., and Robock, A.: Global Cooling After the Eruption of Mount Pinatubo: A  
892 Test of Climate Feedback by Water Vapor, *Science*, 296, 727–730, <https://doi.org/10.1126/science.296.5568.727>,  
893 2002.

894 Sudo, K. and Akimoto, H.: Global source attribution of tropospheric ozone: Long-range transport from various source  
895 regions, *Journal of Geophysical Research Atmospheres*, 112, <https://doi.org/10.1029/2006JD007992>, 2007.

896 Sudo, K., Takahashi, M., Kurokawa, J. I., and Akimoto, H.: CHASER: A global chemical model of the troposphere 1. Model  
897 description, *Journal of Geophysical Research Atmospheres*, 107, ACH 7-1-ACH 7-20,  
898 <https://doi.org/10.1029/2001JD001113>, 2002.

899 Takemura, T., Egashira, M., Matsuzawa, K., Ichijo, H., O’ishi, R., and Abe-Ouchi, A.: A simulation of the global  
900 distribution and radiative forcing of soil dust aerosols at the Last Glacial Maximum, *Atmospheric Chemistry and  
901 Physics*, 9, 3061–3073, <https://doi.org/10.5194/acp-9-3061-2009>, 2009.

902 Tan, Y. B., Peng, L., Shi, Z., and Chen, H. R.: Lightning flash density in relation to aerosol over Nanjing (China),  
903 *Atmospheric Research*, 174–175, 1–8, <https://doi.org/10.1016/j.atmosres.2016.01.009>, 2016.

904 Tang, Y., Rumbold, S., Ellis, R., Kelley, D., Mulcahy, J., Sellar, A., Walton, J., and Jones, C.: MOHC UKESM1.0-LL  
905 model output prepared for CMIP6 CMIP historical, <https://doi.org/10.22033/ESGF/CMIP6.6113>, 2019.

906 Tost, H.: Chemistry–climate interactions of aerosol nitrate from lightning, *Atmospheric Chemistry and Physics*, 17, 1125–  
907 1142, <https://doi.org/10.5194/acp-17-1125-2017>, 2017.

908 Veraverbeke, S., Finney, D., Werf, G. van der, Wees, D. van, Xu, W., and Jones, M.: Global attribution of anthropogenic  
909 and lightning fires, *Copernicus Meetings*, <https://doi.org/10.5194/egusphere-egu22-1160>, 2022.

910 Wang, Q., Li, Z., Guo, J., Zhao, C., and Cribb, M.: The climate impact of aerosols on the lightning flash rate: Is it detectable  
911 from long-term measurements?, *Atmospheric Chemistry and Physics*, 18, 12797–12816, <https://doi.org/10.5194/acp-18-12797-2018>, 2018.

913 Wang, Y., Wan, Q., Meng, W., Liao, F., Tan, H., and Zhang, R.: Long-term impacts of aerosols on precipitation and  
914 lightning over the Pearl River Delta megacity area in China, *Atmospheric Chemistry and Physics*, 11, 12421–12436,  
915 <https://doi.org/10.5194/acp-11-12421-2011>, 2011.

916 Watanabe, S., Hajima, T., Sudo, K., Nagashima, T., Takemura, T., Okajima, H., Nozawa, T., Kawase, H., Abe, M.,  
917 Yokohata, T., Ise, T., Sato, H., Kato, E., Takata, K., Emori, S., and Kawamiya, M.: MIROC-ESM 2010: Model  
918 description and basic results of CMIP5-20c3m experiments, *Geoscientific Model Development*, 4, 845–872,  
919 <https://doi.org/10.5194/gmd-4-845-2011>, 2011.

920 Wild, O.: Modelling the global tropospheric ozone budget: exploring the variability in current models, *Atmospheric  
921 Chemistry and Physics*, 7, 2643–2660, <https://doi.org/10.5194/acp-7-2643-2007>, 2007.

922 Williams, Earle: <https://web.mit.edu/earlerw/www/index.html>, last access: 19 December 2022.

923 Williams, E. R., Weber, M. E., and Orville, R. E.: The relationship between lightning type and convective state of  
924 thunderclouds, *Journal of Geophysical Research: Atmospheres*, 94, 13213–13220,

925 <https://doi.org/10.1029/JD094iD11p13213>, 1989.

926 Yang, X., Yao, Z., Li, Z., and Fan, T.: Heavy air pollution suppresses summer thunderstorms in central China, *Journal of*  
927 *Atmospheric and Solar–Terrestrial Physics*, 95–96, 28–40, <https://doi.org/10.1016/j.jastp.2012.12.023>, 2013.

928 Yuan, T., Remer, L. A., Pickering, K. E., and Yu, H.: Observational evidence of aerosol enhancement of lightning activity  
929 and convective invigoration, *Geophysical Research Letters*, 38, 4701, <https://doi.org/10.1029/2010GL046052>, 2011.

930 Zeng, G., Pyle, J. A., and Young, P. J.: Impact of climate change on tropospheric ozone and its global budgets, *Atmospheric*  
931 *Chemistry and Physics*, 8, 369–387, <https://doi.org/10.5194/acp-8-369-2008>, 2008.

932 Zhao, P., Zhou, Y., Xiao, H., Liu, J., Gao, J., and Ge, F.: Total Lightning Flash Activity Response to Aerosol over China  
933 Area, *Atmosphere*, 8, 26, <https://doi.org/10.3390/atmos8020026>, 2017.

934 Zhao, P., Li, Z., Xiao, H., Wu, F., Zheng, Y., Cribb, M. C., Jin, X., and Zhou, Y.: Distinct aerosol effects on cloud-to-ground  
935 lightning in the plateau and basin regions of Sichuan, Southwest China, *Atmospheric Chemistry and Physics*, 20,  
936 13379–13397, <https://doi.org/10.5194/acp-20-13379-2020>, 2020.

937

938